

# COMPTONIZATION IN SUPER-EDDINGTON ACCRETION FLOW AND GROWTH TIMESCALE OF SUPERMASSIVE BLACK HOLES

TOSHIHIRO KAWAGUCHI<sup>1</sup>

Laboratoire Univers et Théorie, Observatoire de Paris, Section de Meudon, 5 Place Jules Janssen, 92195 Meudon, France;  
 Department of Physics and Astronomy, University of Oklahoma, 440 West Brooks Street, Norman, OK 73019;  
 and Department of Astronomy, Graduate School of Science, Kyoto University, Sakyo-ku, Kyoto 606-8502, Japan;  
 toshihiro.kawaguchi@obspm.fr

Received 2002 October 31; accepted 2003 April 19

## ABSTRACT

Super-Eddington accretion onto black holes (BHs) may occur at ultraluminous compact X-ray sources in nearby galaxies, Galactic microquasars, and narrow-line Seyfert 1 galaxies (NLS1s). Effects of electron scattering (opacity and Comptonization) and the relativistic correction (gravitational redshift and transverse Doppler effect) on the emergent spectra from super-Eddington accretion flows onto non-rotating BHs are examined for  $10^{1.5}$  and  $10^{6.5} M_{\odot}$  BH masses ( $M_{\text{BH}}$ ). With  $\dot{m} \equiv \dot{M}/(L_{\text{Edd}}/c^2) \geq 100$  (where  $\dot{M}$  is the accretion rate), the spectral hardening factor via electron scattering is  $\lesssim 2.3$ – $6.5$ . As a result of the  $\dot{m}$ -sensitive hardening factor, the color temperature of the innermost radiation is not proportional to  $L^{0.25}$ , differing from the simplest standard accretion disk. The model is applied to optical–soft X-ray emission from NLS1s. We pick up one NLS1, namely, PG 1448+273 with an inferred  $M_{\text{BH}}$  of  $10^{6.4} M_{\odot}$ , among the highest  $\dot{m}$  candidates. The broadband spectral distribution is successfully reproduced by the model with an extremely high  $\dot{m}$  ( $=1000$ ) and the viscosity parameter  $\alpha$  of 0.01. This implies that this object, as well as some other highest  $\dot{m}$  systems, is really young: the inferred age,  $M_{\text{BH}}/\dot{M}$ , is about  $10^6$  yr. We also briefly discuss the distribution of  $\dot{m}$  for transient and highly variable NLS1s, finding that those are located at  $3 \lesssim \dot{m} \lesssim 300$ . Such a moderately high accretion rate is indicative of thermal instability. Furthermore,  $\dot{m}$  for a possible type 2 counterpart of NLS1s, NGC 1068, is found to be similar to  $\dot{m}$  for NLS1s.

*Subject headings:* accretion, accretion disks — black hole physics — galaxies: active — galaxies: nuclei — X-rays: galaxies — X-rays: stars

*On-line material:* color figures

## 1. INTRODUCTION

Super-Eddington accretion phenomena onto black holes (BHs) may be important for formation and evolution of supermassive BHs. It may have been much more common in the young universe, when the average BH mass ( $M_{\text{BH}}$ ) would have been smaller than now. Such phenomena are possible sources of UV–extreme-ultraviolet (EUV) photons that may have governed the thermal and star formation history of the universe. Moreover, those extreme accretion rate phases provide us a laboratory in examining our knowledge on accretion phenomena, which have been studied intensively under sub-Eddington regimes (e.g., Shakura & Sunyaev 1973).

Some ultraluminous compact X-ray sources (ULXs) and Galactic microquasars show large bolometric luminosity (greater than or approximately the Eddington luminosity  $L_{\text{Edd}}$  of  $1.4 M_{\odot}$ ) and high color temperature ( $\sim 1$  keV), often referred to as  $T_{\text{in}}$  (e.g., Roberts & Warwick 2000; Makishima et al. 2000; Colbert & Ptak 2002). We note that recent results of ULXs obtained with *XMM-Newton* seem to show lower  $T_{\text{in}}$  ( $\sim 0.15$  keV; Miller et al. 2003). Some possible physical explanations for their nature, including rotating BHs, high accretion rate ( $\dot{M} > L_{\text{Edd}}/c^2$ , where  $\dot{M}$  is the gas accretion rate), intermediate BH mass ( $\sim 100 M_{\odot}$ ), and beamed radiation (see, however, Misra & Sriram 2003), have been discussed.

There is a subclass of active galactic nuclei (AGNs) that are candidates for super-Eddington accretion, namely, narrow-line Seyfert 1 galaxies (NLS1s) and their luminous counterpart, narrow-line QSOs. They are characterized as follows (see Pogge 2000): (1) They have narrower Balmer lines of hydrogen (e.g., FWHM of  $H\beta \leq 2000$  km s<sup>−1</sup>), relative to usual broad-line Seyfert 1 galaxies (BLS1s) and QSOs having FWHM of  $H\beta \gtrsim 5000$  km s<sup>−1</sup> (e.g., Osterbrock & Pogge 1985). (2) They often emit strong optical Fe II multiplets (e.g., Halpern & Oke 1987). (3) Their optical–soft X-ray, big blue bump is hotter than BLS1s/QSOs: they have bluer optical spectra (Grupe et al. 1998) and often show steep and luminous soft X-ray excess (Pounds, Done, & Osborne 1995; Otani, Kii, & Miya 1996; Boller, Brandt, & Fink 1996; Wang, Brinkmann, & Bergeron 1996; Laor et al. 1997; Leighly 1999b). (4) Rapid soft/hard X-ray variability is another characteristic of NLS1s (Otani et al. 1996; Boller et al. 1997; Leighly 1999a; Hayashida 2000). The soft X-ray spectral variability of NLS1s is opposite to that of BLS1s: spectra get harder when they become brighter (Cheng, Wei, & Zhao 2002).

When the luminosity from the accretion disk/flow  $L$  becomes close to  $L_{\text{Edd}}$  [ $L_{\text{Edd}} \sim 1.3 \times 10^{45} (M_{\text{BH}}/10^7 M_{\odot})$  ergs s<sup>−1</sup>], it has been shown that the advective energy transport in the flow dominates over radiative cooling (Abramowicz et al. 1988; § 10.3 of Kato, Fukue, & Mineshige 1998). Such a disk is called an optically thick advection-dominated accretion flow (ADAF) or slim disk,

<sup>1</sup> Postdoctoral Fellow of the Japan Society for the Promotion of Science.

since it is moderately thick geometrically. Abramowicz et al. (1988) showed that  $L$  saturates at around a few times  $L_{\text{Edd}}$  when  $\dot{M}$  exceeds  $L_{\text{Edd}}/c^2$  and that the flow shines even inside the marginally stable orbit,  $3r_{\text{Sch}}$  for nonrotating BHs, where  $r_{\text{Sch}}$  is the Schwarzschild radius and

$$\begin{aligned} r_{\text{Sch}} &\equiv 2GM_{\text{BH}}/c^2 \simeq 3 \times 10^{12} (M_{\text{BH}}/10^7 M_{\odot}) \text{ cm} \\ &= 10^{-3} (M_{\text{BH}}/10^7 M_{\odot}) \text{ lt-days} . \end{aligned}$$

The physical reason why the advection turns on at super-Eddington regime will be the fact that photons cannot escape from the flow before photons/gas are swallowed by the central BH (the photon trapping effect; Begelman & Meier 1982; we discuss it in § 6.2). Slim disk models for ULXs have been constructed to explain high  $T_{\text{in}}$  (Watarai et al. 2000) and mysterious behaviors in  $T_{\text{in}}$  versus  $L_X$  diagrams (Watarai, Mizuno, & Mineshige 2001). Similarly, these models are successful in discussing strong soft X-ray emission (large  $T_{\text{in}}$  relative to other AGNs) and time variability of NLS1s (Mineshige et al. 2000, with  $M_{\text{BH}}$  and  $\dot{M}$  being free parameters). Currently, the most promising picture of NLS1s and narrow-line QSOs is that they contain relatively less massive BHs (with  $M_{\text{BH}} \sim 10^6\text{--}10^8 M_{\odot}$ ) and higher  $L/L_{\text{Edd}}$  (with  $L \sim L_{\text{Edd}}$ ).

As to the emergent spectra from super-Eddington accretion, Szuszkiewicz, Malkan, & Abramowicz (1996) and Wang et al. (1999) considered the opacity due to electron scattering, but without Comptonization or the relativistic correction. Mineshige et al. (2000) and Watarai et al. (2000) simply apply the local blackbody approximation, whereas Watarai et al. (2001) take the spectral hardening factor of 1.7 from Shimura & Takahara (1995) in order to mimic the effect of Comptonization. We note that this factor is derived in the sub-Eddington regime and thus the extent of Comptonization at super-Eddington phase is not evaluated by it (see § 3.2). Self-irradiation and self-occultation are discussed by Fukue (2000) with self-similar solutions of the slim disk model (e.g., Begelman & Meier 1982). Most recently, Wang & Netzer (2003) have studied the effect of Comptonization with self-similar solutions, in order to explain X-ray emission from NLS1s.

A big problem remains when we compare the slim disk model with the observed optical/UV–soft X-ray spectra of NLS1s, namely, the predicted soft X-ray is too steep compared with observations (Szuszkiewicz et al. 1996; Wang et al. 1999).

We examine the effects of electron scattering in opacity, of Comptonization, and of the relativistic correction on spectra from transonic slim accretion flows onto non-rotating BHs, in order to figure out to what extent those effects change the emergent spectrum and whether the effects are enough to fit the observed spectral energy distributions. Now that  $M_{\text{BH}}$  estimations for AGNs are accumulating, we are able to compare the models and observational data with less free parameters than previous studies. We have obtained a promising fit to the broadband energy distribution for the first time. Methods and assumptions of the numerical calculations are given in § 2. We then discuss the physical quantities and emergent spectra of the slim disk in § 3. We turn to the comparison of the model with observed, broadband spectra of NLS1s in § 4. The growth timescale of supermassive BHs is discussed in § 5. In § 6 several discussions are presented. The final section is devoted to a summary.

Throughout the present study we use the normalization  $\dot{M}_{\text{Edd}} (\equiv L_{\text{Edd}}/c^2)$  for  $\dot{M}$ :

$$\begin{aligned} \dot{M}_{\text{Edd}} &\simeq 1.3 \times 10^{18} \left( \frac{M_{\text{BH}}}{10 M_{\odot}} \right) \text{ g s}^{-1} \\ &\simeq 1.3 \times 10^{24} \left( \frac{M_{\text{BH}}}{10^7 M_{\odot}} \right) \text{ g s}^{-1} \\ &\simeq 2.0 \times 10^{-2} \left( \frac{M_{\text{BH}}}{10^7 M_{\odot}} \right) M_{\odot} \text{ yr}^{-1} . \end{aligned} \quad (1)$$

Hereafter  $\dot{m}$  refers to  $\dot{M}/\dot{M}_{\text{Edd}}$ .

Throughout this study, the luminosity is calculated from observed flux assuming isotropic radiation, zero cosmological constant, deceleration parameter  $q_0 = 0.5$ , and Hubble constant  $H_0 = 75 \text{ km s}^{-1} \text{ Mpc}^{-1}$ .

## 2. NUMERICAL PROCEDURES

### 2.1. The Structure of the Accretion Disk

In order to discuss the shape of the emergent spectra from the innermost regions, it is essential to solve the full, derivative equations, rather than the self-similar solutions or other approximate solutions (based on a priori inner boundary conditions or no regularity conditions). The transonic nature of the accretion flow should also be carefully treated.

We solve the steady state, transonic accretion disk structure. The numerical methods are basically the same as those adopted in Matsumoto et al. (1984). The code has been extended for time-dependent simulations (Matsumoto, Kato, & Honma 1989; Honma, Matsumoto, & Kato 1991a; Honma et al. 1991b), and it has been made use of in subsequent papers (Takeuchi 2000; Watarai et al. 2000, 2001; Mineshige et al. 2000). Here we summarize the numerical procedures and briefly describe the basic equations in the following paragraphs. We employ the pseudo-Newtonian potential,  $\psi = -GM/(r - r_{\text{Sch}})$  (Paczynski & Witta 1980), and cylindrical coordinates,  $(r, \varphi, z)$ .

In this study we use vertically integrated (height-averaged) derivative equations. The scale height of the disk  $H$  is comparable to radius  $r$  in the case of extremely large accretion rates  $\dot{M} \gtrsim 100 L_{\text{Edd}}/c^2$ . One may wonder if such a height-averaged approach would not be appropriate. The same problem arises in an optically thin ADAF (Narayan & Yi 1995; see § 10.2 of Kato et al. 1998 and references therein). Narayan & Yi (1995) found that the two-dimensional solutions of the exact non-height-integrated equations agree quite well with those of the simplified height-integrated equations when the “height integration” is done along a constant spherical radius, rather than along  $z$  at constant cylindrical radius (see Narayan 1997). The height-integrated equations therefore are fairly accurate descriptions of quasi-spherical, advective flows.

We construct the vertically integrated equations, using the integrated variables, such as surface density,  $\Sigma \equiv \int \rho dz = 2\bar{\rho}H$ , and integrated total (gas plus radiation) pressure,  $\Pi \equiv \int p dz = 2\bar{p}H$ . Throughout this study (except for the absorption coefficient  $\bar{\kappa}$ ), each quantity with a bar on top means the vertically averaged value, evaluated from the value at the midplane (value with the suffix “mid”):  $\bar{\rho} = (16/35)\rho_{\text{mid}}$ ,  $\bar{p} = (128/315)p_{\text{mid}}$ , and  $\bar{T} = \frac{2}{3}T_{\text{mid}}$ , respectively (Hōshi 1977; see Matsumoto et al. 1984). The scale height of the flow  $H$  is determined by hydrostatic

balance between the vertical gravity and pressure, i.e.,  $H = \Omega_K / c_s$ , where  $c_s$  is the sonic speed. Equations for the conservations of the mass, momentum, and angular momentum are

$$-2\pi r \Sigma v_r = \dot{M} = \text{const}, \quad (2)$$

$$v_r \frac{dv_r}{dr} + \frac{1}{\Sigma} \frac{d\Pi}{dr} = \frac{l^2 - l_K^2}{r^3} - \frac{\Pi}{\Sigma} \frac{d \ln \Omega_K}{dr}, \quad (3)$$

and

$$\dot{M}(l - l_{\text{in}}) = -2\pi r^2 T_{r\varphi}, \quad (4)$$

respectively. Here  $\Omega (= v_\varphi / r)$ ,  $\Omega_K [= (GM/r)^{1/2} / (r - r_{\text{Sch}})]$ ,  $l (= r v_\varphi)$ ,  $l_K (= r^2 \Omega_K)$ , and  $l_{\text{in}}$  are, respectively, the angular frequency of the gas flow, the Keplerian angular frequency in the pseudo-Newtonian potential, the specific angular momentum, the Keplerian angular momentum, and the specific angular momentum finally swallowed by the BH. As to the viscous stress tensor, we adopt the usual prescription  $T_{r\varphi} \equiv -\alpha \Pi$  with the viscosity parameter  $\alpha$ . Unless otherwise noted, we apply  $\alpha$  of 0.1. We neglect self-gravity of the disk, for simplicity. We will see that this is self-consistent with the computed density profile.

The energy budget (per unit surface area) at each radius is symbolically written as

$$Q_{\text{adv}}^- = Q_{\text{vis}}^+ - Q_{\text{rad}}^-, \quad (5)$$

where  $Q_{\text{adv}}^- [\propto \Sigma v_r T (ds/dr)]$  is the advective cooling, with  $s$  being specific entropy, and the other two terms on the right-hand side represent viscous heating and radiative cooling. Assuming that the effective optical depth  $\tau_{\text{eff}}$  is larger than unity, we apply the usual diffusion approximation for  $Q_{\text{rad}}^-$  (see § 3.1):

$$Q_{\text{rad}}^- = \frac{8acT_{\text{mid}}^4}{3\bar{\kappa}\rho_{\text{mid}}H} \approx \frac{Hu_{\text{rad}}}{t_{\text{diff}}}, \quad (6)$$

where the total opacity coefficient is  $\bar{\kappa} = \bar{\kappa}_{\text{abs}} + \bar{\kappa}_{\text{es}}$ . Here  $u_{\text{rad}}$  and  $t_{\text{diff}}$  mean the radiation energy density per unit volume ( $aT^4$ ) and the diffusion timescale of photons (see § 3.1), respectively. This equation describes the photon leakage. Neutrino leakage in proto-neutron stars is discussed in § 6.2. If  $\tau_{\text{eff}}$  gets smaller than unity,  $u_{\text{rad}}$  will be lower than  $aT^4$ . The current cooling rate (eq. [6]) will then overestimate the true cooling rate (Beloborodov 1998). An improvement of the formula, e.g., multiplying the cooling rate by  $(1 - \exp^{-\tau_{\text{eff}}})$ , would be required in the future.

The outer boundary conditions are imposed at  $r = 2.0 \times 10^4 r_{\text{Sch}}$ , where each physical quantity is taken from the formula of the standard disk (Shakura & Sunyaev 1973). The choice of the outer radius does not influence the inner solutions (e.g., Abramowicz et al. 1988). The basic equations are integrated by the semi-implicit method from the outer boundary to the inner one taken at  $r = 2.5 r_{\text{Sch}}$  for  $\dot{m} \leq 10$  and  $1.01 r_{\text{Sch}}$  for  $\dot{m} \geq 100$ . The solutions satisfy the regularity condition at the transonic radius, at about  $2.7 r_{\text{Sch}}$ , and we adopt the free boundary conditions at the inner edge.

The system is taken to be a disk consisting of thermal plasma around a Schwarzschild BH of mass  $M_{\text{BH}}$ . We also assume one-temperature gas (i.e., temperatures of protons and of electrons are the same). The Rosseland mean opacity

is adopted for the absorption opacity  $\bar{\kappa}_{\text{abs}}$ :  $\bar{\kappa}_{\text{abs}} = \bar{\kappa}_{\text{abs},0} \bar{\rho} T^{-3.5}$ . In this study every optical depth is measured between the surface and the midplane of the flow (not from one surface to the other). Generally, the optical depth of absorption  $\tau_{\text{abs}} (H \bar{\rho} \bar{\kappa}_{\text{abs}})$  is much less than that of electron scattering  $\tau_{\text{es}} (H \bar{\rho} \bar{\kappa}_{\text{es}}$ , with the electron scattering opacity  $\bar{\kappa}_{\text{es}}$  of  $0.4 \text{ cm}^2 \text{ g}^{-1}$ ) in the region of interest ( $r \lesssim 10^3 r_{\text{Sch}} - 10^4 r_{\text{Sch}}$ ; see § 3.2 in Kato et al. 1998). The flow is optically thick:  $\tau_{\text{abs}} + \tau_{\text{es}} \gg 1$ . The absorption opacity is an important factor when we are considering whether the effective optical depth of the flow [ $\tau_{\text{eff}} \equiv \sqrt{3} \tau_{\text{abs}} (\tau_{\text{abs}} + \tau_{\text{es}})$ ; Rybicki & Lightman 1979] exceeds unity or not. To estimate the absorption coefficient  $\bar{\kappa}_{\text{abs},0}$  (mainly bound-free transitions for AGN disks with solar abundances; see, e.g., Laor & Netzer 1989), we simply take 30 times the free-free absorption coefficient ( $\bar{\kappa}_{\text{ff},0} = 6.4 \times 10^{22} \text{ cm}^2 \text{ g}^{-1}$ ) for the supermassive BHs, as is done in Czerny & Elvis (1987). For much smaller  $M_{\text{BH}}$  ( $32 M_\odot$ ), we adopt  $\bar{\kappa}_{\text{ff},0}$  as  $\bar{\kappa}_{\text{abs},0}$ . The timescale of Comptonization and that of Coulomb collisions are much shorter than the accretion timescale (Beloborodov 1998).

We neglect the gas evaporation from the disk (e.g., Meyer & Meyer-Hofmeister 1994), since it becomes weak when the gas accretion rate approaches the Eddington limit (Liu et al. 2002). The coronae above and beyond the disk are not included in this study. It will be necessary to consider them when applying the models to hard X-ray spectra (Wang & Netzer 2003).

In total, the input parameters required for the calculations are  $M_{\text{BH}}$ ,  $\dot{M}$ , and  $\alpha$ .

## 2.2. Spectral Calculations

We follow Czerny & Elvis (1987) and Wandel & Petrosian (1988) in dealing with the effect of opacity of electron scattering (i.e., the modified blackbody) and the effect of the energy exchange via Compton scattering (Comptonization). More precise treatments, such as the effects of radiative transfer (see Shimura & Manmoto 2003), will be required for more detailed comparison of models and observations. Given the  $T_{\text{eff}}$ , the local spectrum  $I_\nu(r)$  can be expressed by  $I_\nu(r) = B_\nu(T) f_\nu(T, r)$ , where  $B_\nu(T)$  is the Planck function. Here  $f_\nu(T, r)$  is

$$f_\nu(T, r) = \frac{2[1 - \exp^{-\tau_{\text{eff}}(T, r)}]}{1 + \sqrt{[\tau_{\text{abs},\nu}(T, r) + \tau_{\text{es}}(r)] / \tau_{\text{abs},\nu}(T, r)}}, \quad (7)$$

where  $\tau_{\text{abs},\nu}(T, r)$  is the optical thickness for absorption with a given temperature  $T$  at frequency  $\nu$  and the effective optical depth  $\tau_{\text{eff},\nu}(T, r)$  is computed as

$$\{3\tau_{\text{abs},\nu}(T, r)[\tau_{\text{abs},\nu}(T, r) + \tau_{\text{es}}(r)]\}^{1/2}.$$

The parentheses including the exponential term take into account the finite, effective optical depth of the flow. For low  $\tau_{\text{eff},\nu}(T, r) (\ll 1)$ , it describes the thermal bremsstrahlung from an optically thin medium. If the absorption opacity dominates over the opacity of electron scattering (and if the flow is effectively optically thick),  $f_\nu(T, r)$  is unity. The color temperature  $T$  is determined so that the surface emissivity does not change:  $\int_0^\infty d\nu I_\nu(r) \equiv acT_{\text{eff}}^4/4\pi$ .

A simple evaluation of the spectral hardening factor due to the modified blackbody is (Madej 1974)

$$\log_{10} \left( \frac{T_{\text{rmcol}}}{T_{\text{rmeff}}} \right) \simeq -\frac{1}{8} \log_{10} \left( \frac{\tau_{\text{abs}}}{\tau_{\text{abs}} + \tau_{\text{es}}} \right). \quad (8)$$



Compton scattering is important when the Compton parameter  $y = (4k\bar{T}/m_e c^2) \max(\tau_{\text{es}}, \tau_{\text{es}}^2)$  is greater than 1. However, below the last thermalization surface, where the effective optical depth measured from the surface equals unity, the energy exchange via Compton scattering will be statistically canceled as a result of the efficient absorption. Scattering above the surface is in question. Then, the relevant opacity for electron scattering,  $\tau'_{\text{es}}$ , will be  $\tau_{\text{es}}/\tau_{\text{eff}}$  for  $\tau_{\text{eff}} > 1$  and  $\tau_{\text{es}}$  for  $\tau_{\text{eff}} < 1$ :

$$\tau'_{\text{es}} = \frac{\tau_{\text{es}}}{\max(\tau_{\text{eff}}, 1)}. \quad (9)$$

Finally, the effective Compton  $y$  parameter  $y_*$  is

$$y_* = \frac{4k\bar{T}}{m_e c^2} \max(\tau'_{\text{es}}, \tau_{\text{es}}^2). \quad (10)$$

Comptonization will considerably modify the emergent spectrum if  $y_* > 1$ . The radial distribution of  $y_*$  increases inward steeply, reaching a maximum at  $\sim 3r_{\text{Sch}} - 5r_{\text{Sch}}$ , and it decreases inward (Wandel & Petrosian 1988). In the regime for which  $\tau_{\text{es}} \gg \tau_{\text{abs}}$  and  $\tau_{\text{eff}} > 1$ ,

$$y_* \propto \bar{T}^{4.5} \bar{\rho}^{-1} \left( \frac{\bar{\kappa}_{\text{abs},0}}{\bar{\kappa}_{\text{ff},0}} \right)^{-1}, \quad (11)$$

yielding a strong temperature dependency.

Photons generated at large optical depth undergo many scatterings and change their energy as a result of Comptonization. The effect on emergent spectra can be estimated by assuming that a fraction  $f_{\text{th},\nu}$  of the photons at frequency  $\nu$  are shifted and cumulated into a Wien peak of an average energy  $3kT$ . For a given frequency  $\nu$ , the fraction of these thermalized photons to all generated photons  $f_{\text{th},\nu}$  is given as

$$f_{\text{th},\nu} = \exp \left\{ - \frac{\ln(kT/h\nu)}{\tau_{\text{es}}^2 \ln \left[ 1 + 4kT/m_e c^2 + 16(kT/m_e c^2)^2 \right]} \right\} \quad (12)$$

(Svensson 1984), if the absorption is negligible. For high-energy photons ( $kT < h\nu$ ),  $f_{\text{th},\nu}$  would be able to exceed unity. We therefore put a constraint so that  $f_{\text{th},\nu} \leq 1.0$ . Since the redistribution of low-energy photons into Wien peak is the problem, this artificial constraint on high-energy photons will be a reasonable approximation (cf. Wandel & Petrosian 1988). Equation (12) can be adapted to a more general case if  $\tau_{\text{es}}$  in the equation is replaced by the total optical depth  $\tau_{\nu}^{\text{total}}$  (Czerny & Elvis 1987):

$$\tau_{\nu}^{\text{total}} = \frac{\tau_{\text{es}} + \tau_{\text{abs},\nu}}{1 + \tau_{\text{eff}}} \approx \begin{cases} \tau_{\text{es}} & \text{for } \tau_{\text{eff}} \ll 1, \tau_{\text{es}} \gg \tau_{\text{abs}}, \\ \tau_{\text{es}}^{1/2} \tau_{\text{abs}}^{-1/2} & \text{for } \tau_{\text{eff}} \gg 1, \tau_{\text{es}} \gg \tau_{\text{abs}}. \end{cases} \quad (13)$$

The removed photons will result in a total additional energy output (we use  $2.7kT$  instead of  $3kT$ , following Wandel & Petrosian 1988)

$$I_{\text{th},\nu} = 2.7kT \int_0^\infty d\nu f_{\text{th},\nu} \frac{I_\nu}{h\nu}. \quad (14)$$

The distribution of the shifted photons around the Wien peak is approximated by a blackbody spectrum with a

normalization constant  $C$  given by

$$I_{\text{th},\nu} \approx \frac{CacT^4}{4\pi}. \quad (15)$$

As a whole, the deviation of the emitted spectrum from a blackbody is finally described as

$$f_\nu(T, r) = \frac{2[1 - \exp^{-\tau_{\text{eff}}(T, r)}]}{1 + \sqrt{[\tau_{\text{abs},\nu}(T, r) + \tau_{\text{es}}(r)]/\tau_{\text{abs},\nu}(T, r)}} \times (1 - f_{\text{th},\nu}) + C, \quad (16)$$

instead of  $f_\nu(T, r)$  in equation (7). Again, the temperature  $T$  ( $\geq T_{\text{eff}}$ ) is adjusted to reproduce the original surface emissivity, so that the luminosity of the flow is conserved. As the result, the emergent spectra become harder than spectra based on the local blackbody approximation [ $B_\nu(T_{\text{eff}})$ ; Czerny & Elvis 1987; Wandel & Petrosian 1988]. A hot surface layer will arise whose temperature  $T$  is much larger than  $T_{\text{eff}}$ , as seen in standard disks with  $\dot{m} > 1$  (Shimura & Takahara 1993).

Next, we add the effects of the relativistic correction on the effective temperature  $T_{\text{eff}}$  and emergent spectra. Since only the gravitational redshift and transverse Doppler shift (i.e., no Doppler boosting) are considered, the computational results correspond to face-on views of the flow. We assume that the rotational velocity  $v_\phi$  is almost the same as the Keplerian velocity  $v_K$ . The consistency will be shown later with the calculated velocity field (§ 3.1). We employ the relativistic correction for the Keplerian disk (e.g., Kato et al. 1998, § 3.5.3):

$$(1 + z_{\text{rc}}) = \left( 1 - \frac{3r_{\text{Sch}}}{2R} \right)^{-1/2}. \quad (17)$$

We take  $1 + z_{\text{rc}} = [\max(10^{-3}, 1 - 3r_{\text{Sch}}/2R)]^{-1/2}$ , for the moment. The effective temperature  $T_{\text{eff}}$  becomes lower by  $(1 + z_{\text{rc}})^{-1}$  [i.e., emissivity per surface area decreases by  $(1 + z_{\text{rc}})^{-4}$ ], compared with the cases without the relativistic correction (e.g., Watarai et al. 2000, 2001; Mineshige et al. 2000).

We have applied this expression to describe the shape of the radiation spectrum emitted at every radius of the disk.

### 3. NUMERICAL RESULTS

In this section we show the basic physical quantities in the accretion flow and emergent spectra for  $M_{\text{BH}}$  of  $10^{6.5} M_\odot$  and  $\alpha = 0.1$ . For AGNs ( $M_{\text{BH}} \gtrsim 10^6 M_\odot$ ),  $M_{\text{BH}}$  is now estimated by a couple of methods, and both the inner and outer radii are observable at X-ray and optical/UV bands. We chose  $\alpha$  of 0.1 in order to compare the  $T_{\text{eff}}(r)$  profile and the resultant spectra with those in Mineshige et al. (2000). We also describe briefly the  $\alpha$  dependency using the  $\alpha = 0.01$ ,  $10^{-3}$  results, as well as the  $M_{\text{BH}}$  dependency comparing with  $10^{1.5}$  ( $=32$ )  $M_\odot$  BH results.

#### 3.1. Physical Quantities of the Flow

Figure 1 exhibits the opacity of electron scattering ( $\tau_{\text{es}}$ ), that of absorption ( $\tau_{\text{abs}}$ ), and the effective opacity ( $\tau_{\text{eff}}$ ). Here  $M_{\text{BH}}$  and  $\alpha$  are chosen as  $10^{6.5} M_\odot$  and 0.1, respectively. The figure clearly shows that  $\tau_{\text{es}}$  (solid lines) at  $r \lesssim 100r_{\text{Sch}}$  is larger than  $\tau_{\text{abs}}$  (dotted lines) by several orders for all the  $\dot{m}$  (1–1000). The deviation is much more

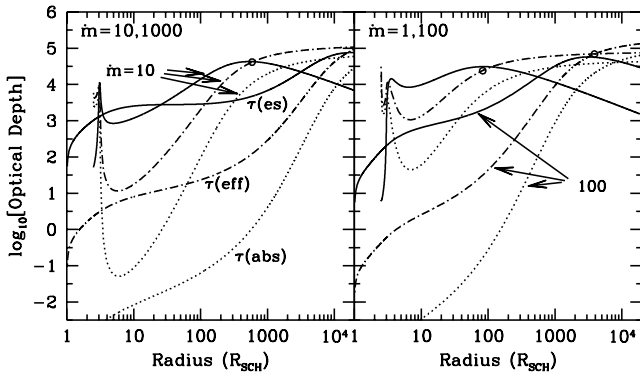


FIG. 1.—Opacity of electron scattering ( $\tau_{\text{es}}$ ; solid lines), that of absorption ( $\tau_{\text{abs}}$ ; dotted lines), and the effective opacity ( $\tau_{\text{eff}}$ ; dot-dashed lines). Here  $M_{\text{BH}}$  and  $\alpha$  are chosen to be  $10^{6.5} M_{\odot}$  and 0.1, respectively. It is shown that  $\tau_{\text{es}}$  is larger than  $\tau_{\text{abs}}$  by several orders at  $r \lesssim 10r_{\text{Sch}}$  for all the  $\dot{m}$  (1–1000). The left-hand panel is drawn for  $\dot{m} = 10$  and 1000, while the right-hand panel is for  $\dot{m} = 1$  and 100. Open circles indicate the position where  $p_{\text{rad}} = p_{\text{gas}}$ . Inner parts are  $p_{\text{rad}}$ -dominated regions. With  $\dot{m} = 1000$ , the entire region presented here is  $p_{\text{rad}}$  dominated. [See the electronic edition of the Journal for a color version of this figure.]

prominent in the super-Eddington phases than in the sub-Eddington phase ( $\dot{m} \lesssim 10$ ). Therefore, the local blackbody approximation must be modified, especially in the super-Eddington cases, in which  $\tau_{\text{es}}$  enormously dominates over  $\tau_{\text{abs}}$  (see eq. [8]). With  $\dot{m} \sim 100$ ,  $\tau_{\text{eff}} \leq 1$  at  $r \lesssim 4r_{\text{Sch}}$ . Thus, the diffusion approximation for the cooling rate (eq. [6]) will not be valid around this  $\dot{m}$ . We will therefore search for objects with even higher  $\dot{m}$  in § 4.1. The surface density  $\Sigma$  is proportional to  $\tau_{\text{es}}$ ;  $\Sigma$  decreases with an increasing  $\dot{m}$  as far as  $\dot{m} \leq 100$ . As  $\dot{m}$  increases from 100 to 1000,  $\Sigma$  conversely increases (since  $v_r$  increases only slightly) and the density at the inner region ( $r \lesssim 50r_{\text{Sch}}$ ) is also enlarged: both  $\tau_{\text{es}}$  and  $\tau_{\text{abs}}$  get larger. Consequently, the effective optical depth with  $\dot{m} = 1000$  recovers to above unity. Open circles exhibit the radii where the radiative pressure ( $a\bar{T}^4/3$ ) equals the gas pressure ( $2k_B\bar{\rho}\bar{T}/m_H$ ). The former dominates over the latter within the inner region. The  $\dot{m}$  dependency of the radius is similar to the standard disk ( $\propto \dot{m}^{16/21}$ ).

We present the effective Compton  $y$  parameter  $y_*$  (eq. [10]) for various accretion rates. Each solid line in Figure 2 shows the distribution of  $y_*$  as a function of radius  $r$ . The horizontal dotted line means  $y_*$  of unity, above which the spectral distortion due to Comptonization is crucial. The large increase of  $y_*$  along with the increase of  $\dot{m}$  arises from a decrease of  $\bar{\rho}$  and an increase of  $\bar{T}$  from  $\dot{m} = 10$  to 100–1000 (see Fig. 5). Since  $\bar{\rho} \propto M_{\text{BH}}^{-1}$  and  $\bar{T} \propto M_{\text{BH}}^{-1/4}$  (as will be shown later), it is quite difficult to achieve a large  $y_*$  ( $\propto \bar{T}^{4.5}\bar{\rho}^{-1}$ ; eq. [11]) with sub-Eddington accretion rates for all relevant  $M_{\text{BH}}$ . In other words, the huge  $y_*$  ( $\gg 1$ ) is obtainable only for super-Eddington cases.

We assume Keplerian rotation for the transverse Doppler effects (§ 2.2). Figure 3 shows that the transverse velocity  $v_{\phi}$  is almost equivalent to the Keplerian velocity  $v_K$  ( $v_{\phi} \gtrsim 0.8v_K$ ) up to the extremely large  $\dot{m}$  (1000) cases. Thus, the assumption is not very bad. The radial velocity  $v_r$  increases with a larger  $\dot{m}$  (bottom panel). This is the reason behind the ignition of the photon trapping in the super-Eddington accretion. In the extreme super-Eddington cases ( $\dot{m} \gtrsim 1000$ ),  $v_r$  in the innermost region ( $r \lesssim 10r_{\text{Sch}}$ ) is about 10% of the Keplerian one (i.e.,  $v_r \propto \alpha v_K$ ). Thus, the inner flow could be more time variable than lower  $\dot{m}$  cases. In the

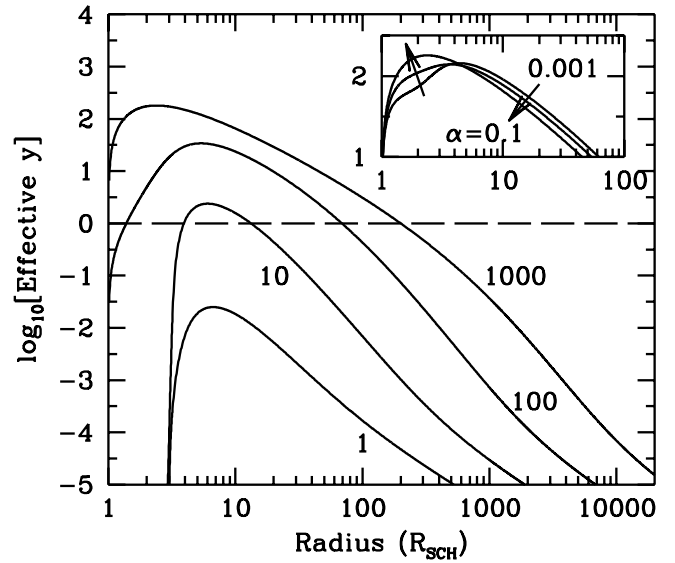


FIG. 2.—Effective Compton  $y$  parameter,  $y_*$ , for various  $\dot{m}$ . A long-dashed line means that  $y_* = 1$ , above which Comptonization is very important on the spectral calculations. It is clear that  $y_*$  with super-Eddington accretion rate is much larger than the cases with sub-Eddington accretion. The inset shows the  $\alpha$  dependency of  $y_*$  for  $\dot{m} = 1000$ :  $\bar{\rho}$  increases with smaller  $\alpha$ , and then  $y_*$  at the innermost region decreases. [See the electronic edition of the Journal for a color version of this figure.]

extreme limit of advection-dominated flow ( $\dot{Q}_{\text{adv}} \gg \dot{Q}_{\text{rad}}^-$ ), the radial velocity  $v_r$  is expected to be  $\sim 0.4\alpha v_K$  (e.g., Fukue 2000). Filled circles indicate the location of the sonic point, where  $v_r$  equals the sound speed  $c_s$ . The sonic points are located around  $3r_{\text{Sch}}$  for all  $\dot{m}$ , consistent with the  $\alpha = 0.1$  cases in Abramowicz et al. (1988).

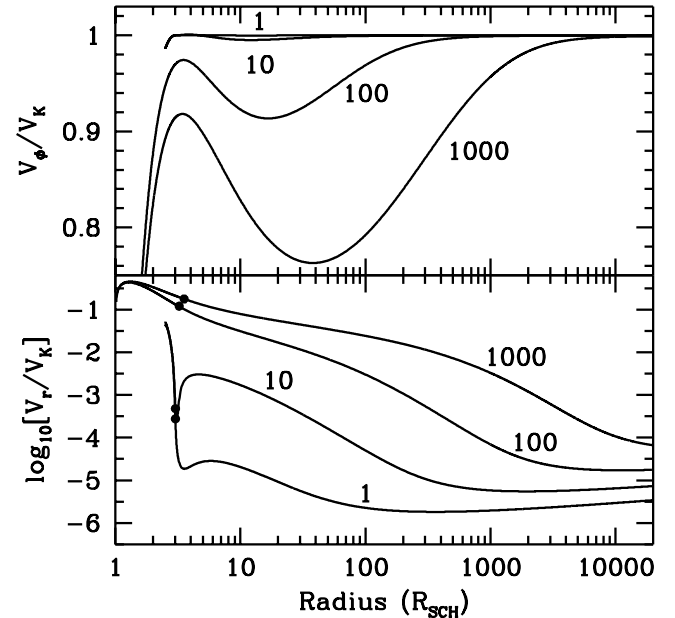


FIG. 3.—Azimuthal velocity (top) and radial velocity (bottom) in the unit of the Keplerian velocity  $v_K$  as functions of radius. The rotation is almost Keplerian for all the  $\dot{m}$  here, within  $\sim 20\%$  deviation at most. The radial velocity increases drastically with increasing  $\dot{m}$ : it reaches  $\sim 10\%$  of the Keplerian velocity for  $\dot{m} = 1000$  at the inner region ( $r \lesssim 10r_{\text{Sch}}$ ). Filled circles indicate the location of the sonic points ( $v_r/c_s = 1$ ) for each parameter set, where the sonic speed  $c_s$  is calculated as  $\sqrt{\bar{p}/\bar{\rho}}$ . [See the electronic edition of the Journal for a color version of this figure.]

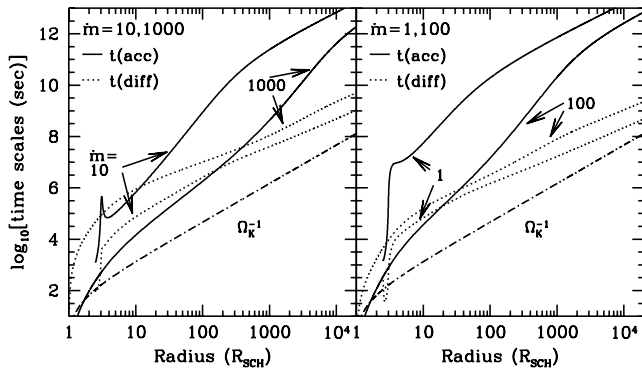


FIG. 4.—Accretion timescale [ $t_{\text{acc}} = (r - r_{\text{Sch}})/v_r$ ; solid lines] and diffusion timescale of photons [ $t_{\text{diff}} = H(\tau_{\text{es}} + \tau_{\text{abs}})/c$ ; dotted lines] for the slim accretion disk model. The viscosity parameter  $\alpha$  is 0.1 here. The switch of the two timescales happens at  $\dot{m}$  between 10 and 100. The dot-dashed lines mean the vertical, hydrodynamical timescale [ $H/c_s = \Omega_K^{-1} = 255(M_{\text{BH}}/10^7 M_\odot)(r/3r_{\text{Sch}})^{0.5}(r/r_{\text{Sch}} - 1)$  s for the pseudo-Newtonian potential]. [See the electronic edition of the Journal for a color version of this figure.]

Next, we compare the timescales of accretion [ $t_{\text{acc}}$  defined as  $(r - r_{\text{Sch}})/v_r$ ] with that of diffusion of photons from mid-plane to the surface of the disk [ $t_{\text{diff}} \equiv H(\tau_{\text{es}} + \tau_{\text{abs}})/c$ ]. Figure 4 shows that  $t_{\text{acc}}$  is larger than  $t_{\text{diff}}$  everywhere for  $\dot{m} \leq 10$ , while it is not always true for  $\dot{m} \geq 100$ . The switch of the two timescales happens between  $\dot{m}$  of 10 and 100. Advective cooling (photon trapping) begins to take place from the inner region. For example, the outer part ( $r > 40r_{\text{Sch}}$  for  $\dot{m} = 100$  and  $R > 400r_{\text{Sch}}$  for  $\dot{m} = 1000$ ) does not suffer from the effects of photon trapping. Those radii can be analytically derived as  $0.5\dot{m}$  (Begelman & Meier 1982). It is also clear that the accretion timescale at a fixed radius decreases drastically with increasing  $\dot{M}$ . In super-Eddington cases, the structure of the inner accretion flow can be highly time variable. The timescale for achieving the vertical hydrostatic balance,  $H/c_s = \Omega_K^{-1}$ , is always much shorter than  $t_{\text{acc}}$ .

The scale height of the flow  $H$  in the unit of radius  $r$  is shown in Figure 5 (top panel). The aspect ratio  $H/r$  increases with  $\dot{M}$ , being geometrically thick ( $H/R \gtrsim 0.5$ ) at  $\dot{m} \gtrsim 100$ . We shall discuss this issue later when we are seeking ideal objects to test the model (§ 4.1). Moreover, the shape of  $H/R$  shows that the heating by the irradiation from the innermost part of the flow onto the outer radii ( $\gtrsim 10^4 r_{\text{Sch}}$ ) is negligible. The radial profile of the mean density  $\bar{\rho}$  is also shown (solid lines in the second panel). As Beloborodov (1998) noted,  $\bar{\rho}$  at  $r \lesssim 50r_{\text{Sch}}$  has a minimum at  $\dot{m} \sim 100$ . Here the dot-dashed line indicates a critical density,  $\rho(\text{sg}, z)$ , above which self-gravity of the disk in the vertical ( $z$ ) direction must be considered:

$$\begin{aligned} \rho(\text{sg}, z) &= \frac{\Omega_K^2}{4\pi G} \\ &= 18 \left( \frac{M_{\text{BH}}}{10^7 M_\odot} \right)^{-2} \left( \frac{r}{3r_{\text{Sch}}} \right)^{-1} \left( \frac{r}{r_{\text{Sch}}} - 1 \right)^{-2} \text{ g cm}^{-3}. \end{aligned} \quad (18)$$

As  $\dot{m}$  increases, the relative importance of self-gravity [ $\rho(\text{sg}, z)/\bar{\rho}$ ] in the outer region is enhanced. With  $\dot{m} > 1000$ , the outer part of the flow [ $r \gtrsim 2 \times 10^4 r_{\text{Sch}} \simeq 0.006(M_{\text{BH}}/10^{6.5} M_\odot) \text{ pc}$ ] will form a self-gravitating disk. Objects with super-Eddington accretion rate are therefore good labora-

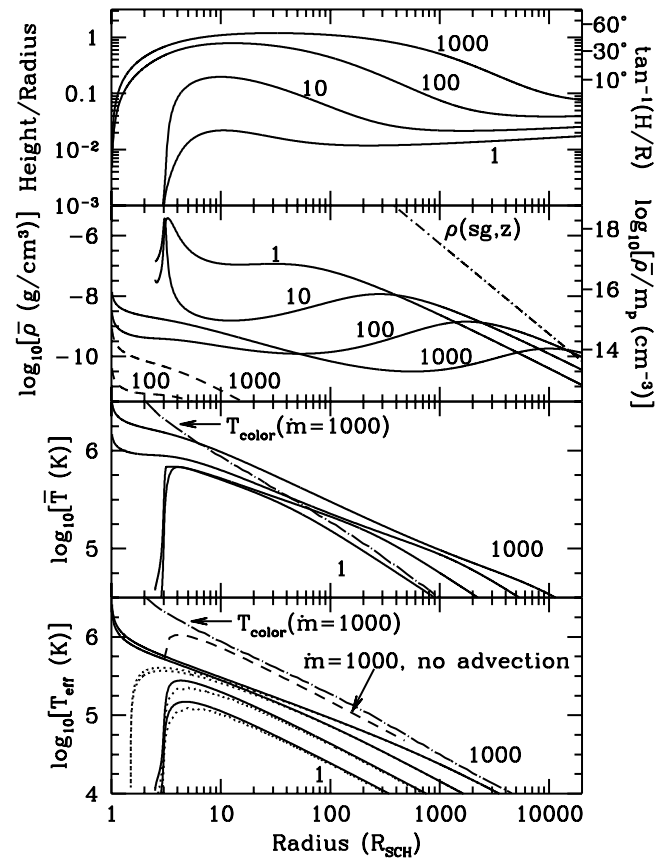


FIG. 5.—Examples of  $\dot{m}$  dependency of the physical quantities. The corresponding  $\dot{m}$  are labeled. First, the scale height of the flow (from the midplane to the surface) divided by the radius is shown (top). The second panel exhibits the radial profile of the mean density  $\bar{\rho}$  by solid lines. The dot-dashed line indicates a critical density,  $\rho(\text{sg}, z)$ , above which self-gravity of the disk in the vertical ( $z$ ) direction must be considered. The lower two dashed lines represent the inertia of the heat,  $\rho_{\text{rad}}$ , for  $\dot{m} = 100$  and 1000. The third panel depicts the mean temperature  $\bar{T}$ . In the bottom panel, the effective temperature profiles  $T_{\text{eff}}(r)$  before the relativistic correction (solid lines) are compared with those with the correction (dotted lines; eq. [17]). The dashed line also shows  $T_{\text{eff}}(r)$ , but it is the case with no advection (i.e.,  $Q_{\text{vis}}^+ = Q_{\text{rad}}^-$ ). Because of the relativistic correction, the maximum  $T_{\text{eff}}$  of the slim disk is less than that of the  $Q_{\text{vis}}^+ = Q_{\text{rad}}^-$  case. Dot-long-dashed lines in the third and bottom panels present the color temperature derived with eq. (16) for the  $\dot{m} = 1000$  case. The spectral hardening factor can be estimated from the ratio of the color temperature to the effective temperature. [See the electronic edition of the Journal for a color version of this figure.]

tories for studying the self-gravity of accretion flows by optical/near-infrared (NIR) observations. Quantitative details will be shown in a future paper (Kawaguchi, Pierens, & Huré 2003). Another critical density for radial self-gravity,  $\rho(\text{sg}, r)$ , is  $16\rho(\text{sg}, z)$  (Goldreich & Lynden-Bell 1965; see Huré 1998 for a review). The inertia of the heat (Beloborodov, Abramowicz, & Novikov 1997; dashed lines in the second panel) is always much smaller than the gas rest-mass density  $\bar{\rho}$  in this study (disks around nonrotating BHs):  $\rho_{\text{rad}} \equiv a\bar{T}^4/c^2 \simeq 10^{-11}(\bar{T}/10^6 \text{ K})^4 \text{ g cm}^{-3} \ll \bar{\rho}$  (third panel).

Finally, the effective temperature profiles  $T_{\text{eff}}(r)$  before the relativistic correction (solid lines) are compared with those with the correction (dotted lines; eq. [17]). Although the flow with  $\dot{m} > 100$  extends much closer to the central BHs than lower  $\dot{m}$  cases, those regions are not as luminous as thought in previous papers (Watarai et al. 2000, 2001; Mineshige et al. 2000). If the system is not face-on, the discrepancy of the two profiles shrinks as a result of the



Doppler boosting and the reduction of the transverse Doppler effect. Viewing angle-dependent spectra are needed for investigation in the future. The dashed line also shows  $T_{\text{eff}}(r)$ , but it is derived without advection (i.e.,  $Q_{\text{vis}}^+ = Q_{\text{rad}}^-$ ):

$$T_{\text{eff}}(r) = 6.2 \times 10^5 \left( \frac{M_{\text{BH}}}{10^7 M_{\odot}} \right)^{-1/4} \left( \frac{\dot{M}}{L_{\text{Edd}}/c^2} \right)^{1/4} \times \left( \frac{r}{r_{\text{Sch}}} \right)^{-3/4} \left( 1 - \sqrt{\frac{3r_{\text{Sch}}}{r}} \right)^{1/4} \text{ K}. \quad (19)$$

As a result of the relativistic correction, the maximum  $T_{\text{eff}}$  of the slim disk becomes less than that of the  $Q_{\text{vis}}^+ = Q_{\text{rad}}^-$  case. Dot-long-dashed lines in the third and bottom panels present the color temperature derived with equation (16) for the  $\dot{m} = 1000$  case.

Since we shall use the spectra with  $\alpha$  of 0.01 ( $M_{\text{BH}} = 10^{6.5} M_{\odot}$ ) when testing our model with the observed spectrum, we here briefly discuss the  $\alpha$  dependency of the flow. The  $\alpha$  dependencies of all the physical quantities (Figs. 1–5) are almost the same as the standard disk; i.e.,  $\tau_{\text{es}}(\propto \Sigma) \propto \alpha^{-1}$ ,  $v_r \propto \alpha$ ,  $t_{\text{acc}} \propto \alpha^{-1}$ ,  $t_{\text{diff}} \propto \alpha^{-1}$ ,  $H/r \propto \alpha^0$ ,  $\bar{\rho} \propto \alpha^{-1}$ ,  $\bar{T} \propto \alpha^{-0.25}$ , etc. The exception arises at the innermost region,  $r \leq 10r_{\text{Sch}}$ , namely,  $\tau_{\text{es}}(\propto \Sigma)$ ,  $v_r$ , and the two timescales at  $r \leq 1.5r_{\text{Sch}}$  are unchanged. The transition between the two different  $\alpha$  dependencies occurs at  $1.5 \leq r \leq 10r_{\text{Sch}}$ . The effective Compton  $y$  parameters for the three values of  $\alpha$  (with  $\dot{m} = 1000$ ) are drawn in the inset of Figure 2, showing the decrease of  $y_*$  at  $r \lesssim 4r_{\text{Sch}}$  with decreasing  $\alpha$ . Figure 6 depicts the aspect ratio (*top panel*),  $\bar{\rho}$  (*second panel*),  $\bar{T}$  (*third panel*), and  $T_{\text{eff}}$  (*bottom panel*) for different  $\alpha$  (0.1, 0.01,  $10^{-3}$ ) with  $M_{\text{BH}} = 10^{6.5} M_{\odot}$  and  $\dot{m} = 1000$ . The behavior of  $\bar{T}$  of the inner region is the opposite of that of the outer part. Lower  $\alpha$  makes the self-gravity of the flow more important at outer radii. The sonic point approaches the center with decreasing  $\alpha$ , as shown in Abramowicz et al. (1988). With smaller  $\alpha$ ,  $\bar{T}(r)$  tends to have a hump, so that the pressure gradient  $[d\Pi/dr \propto d(H\bar{T}^4)/dr]$  pushes the gas toward the central BH more strongly. The  $\alpha$  dependency of  $T_{\text{eff}}(r)$  is shown in Watarai & Mineshige (2001).

Computations for  $M_{\text{BH}} = 32 M_{\odot}$  are also made in order to (1) assess the  $M_{\text{BH}}$  dependency, (2) apply the present model to ULXs/microquasars, and (3) compare our spectra with those in Shimura & Takahara (1995) in the sub-Eddington regime. Although the  $\dot{m}$  dependency of the quantities (Figs. 1–5) in the slim disk is different from that in the standard disk, the  $M_{\text{BH}}$  dependency is almost identical: e.g.,  $H/r \propto M_{\text{BH}}^0$ ,  $\bar{\rho} \propto M_{\text{BH}}^{-1}$  (at the  $p_{\text{rad}}$ -dominated region),  $\bar{T}$  ( $p_{\text{rad}}$  region) and  $T_{\text{eff}}$  are proportional to  $M_{\text{BH}}^{-1/4}$ ,  $t_{\text{acc}}$  and  $t_{\text{diff}}$  ( $p_{\text{rad}}$  region) are proportional to  $M_{\text{BH}}$ . The radius (in the unit of  $r_{\text{Sch}}$ ) at which  $p_{\text{rad}} = p_{\text{gas}}$  is proportional to  $M_{\text{BH}}^{2/21}$ .

Different values of the ratio ( $\bar{\kappa}_{\text{abs},0}/\bar{\kappa}_{\text{ff},0}$ ) are used in different  $M_{\text{BH}}$  cases (§ 2.1); thus, the absorption-dominated region is located farther out than for  $M_{\text{BH}} = 10^{6.5} M_{\odot}$ . Because of the change of the absorption coefficient, it gets easier for the flow to have  $\tau_{\text{eff}}$  less than unity:  $\tau_{\text{eff}} \leq 1$  at  $r \leq 10r_{\text{Sch}}$  for  $\dot{m} = 100$  and at  $r \leq 3r_{\text{Sch}}$  for  $\dot{m} = 1000$ . Comparing with  $10^{6.5} M_{\odot}$  BHs,  $y_*$  is enlarged by a factor of  $\sim 100$  at all radii and all the  $\dot{m}$ . The changes of  $\bar{\rho}$  and  $\bar{T}$  due to the decrease of  $M_{\text{BH}}$  by 5 orders result only in 0.6 order increase of  $y_*$  (eq. [11]). The rest ( $\sim 1.5$  orders) arises from the decrease of ( $\bar{\kappa}_{\text{abs},0}/\bar{\kappa}_{\text{ff},0}$ ). Since  $\rho(\text{sg}, z) \propto M_{\text{BH}}^{-2}$ , self-gravity of the disk around  $32 M_{\odot}$  BHs is not important at

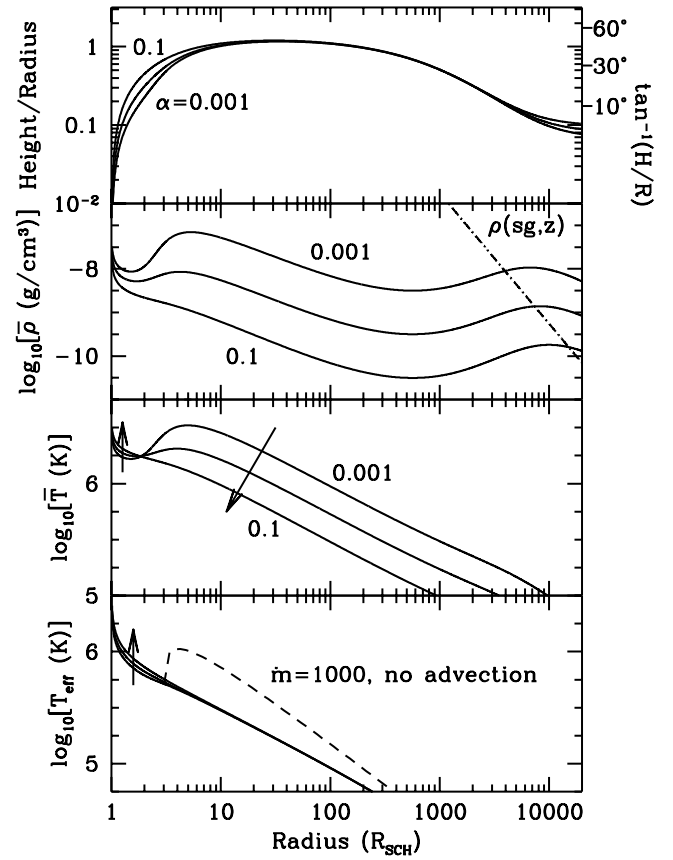


FIG. 6.—Aspect ratio (*top panel*),  $\bar{\rho}$  (*second panel*),  $\bar{T}$  (*third panel*), and  $T_{\text{eff}}$  (*bottom panel*) for different  $\alpha$  (0.1, 0.01, and  $10^{-3}$ ) with  $M_{\text{BH}} = 10^{6.5} M_{\odot}$  and  $\dot{m} = 1000$  cases. The  $\alpha$  dependency of the physical quantities is almost the same as the standard disk, except for the innermost region,  $r \lesssim 10r_{\text{Sch}}$ . The behavior of  $\bar{T}$  of the inner region with varying  $\alpha$  is the opposite of that of the outer part. Arrows mean the evolution with increasing  $\alpha$ . [See the electronic edition of the *Journal* for a color version of this figure.]

all. Instead, it gets more significant with larger  $M_{\text{BH}}$ . Again,  $\rho_{\text{rad}}$  is always negligible.

### 3.2. Emergent Spectra

Figure 7 shows each effect of spectral calculation on the emergent spectrum for the case of  $\dot{m} = 1000$  and  $\alpha = 0.1$ . First, the dotted line represents the case with no advection: all the dissipated energy goes into radiation as in the standard accretion disks. For this curve, we put the inner radius at  $3r_{\text{Sch}}$ . The long-dashed line exhibits the spectrum with advection based on transonic accretion flow (i.e., the same as Mineshige et al. 2000, except for the face-on view here). We note that the local spectrum is still assumed as black-body radiation here. Next, we take into account the relativistic correction at the innermost region of the flow (*dot-dashed line*). The flow extends inside the last stable orbit ( $3r_{\text{Sch}}$ ; e.g., Abramowicz et al. 1988; Watarai et al. 2000; Mineshige et al. 2000). However, the emission from those regions, where gravity is extraordinarily strong and azimuthal velocity is relativistic, is drastically suppressed by the gravitational redshift and transverse Doppler redshift. As the result, the color temperature of the inner region (where the highest energy photons are emitted) decreases by a factor of  $\sim 5.7$ . We should stress here that the bolometric luminosity of the flow  $L$  is not very large in spite of the

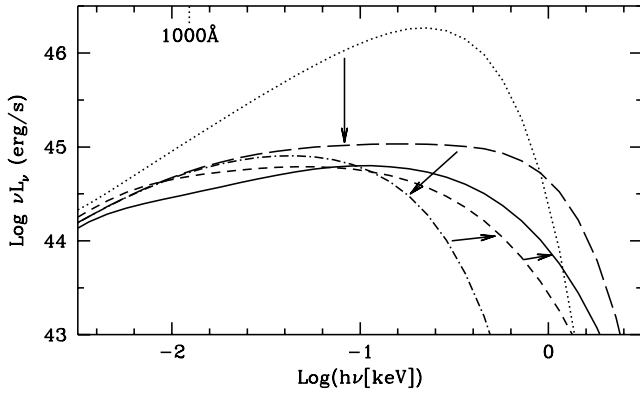


FIG. 7.—Each effect on the emergent spectrum for  $\dot{m} = 1000$ . The dotted line represents the case with no advection (as in the standard accretion disks) with an assumed inner radius at  $3r_{\text{Sch}}$ . Then, the long-dashed line exhibits the spectrum with advection based on the transonic accretion flow (i.e., the same as Mineshige et al. 2000, except for face-on view here), and the bolometric luminosity of the flow  $L$  is about  $5.1L_{\text{Edd}}$ . The local spectrum is still assumed as blackbody radiation here. Next, we take into account the relativistic correction at the innermost region of the flow (*dot-dashed line*). As a result, the color temperature of the emission from the innermost region decreases by a factor of  $\sim 5.7$  and  $L$  becomes  $2.6L_{\text{Edd}}$ . Moreover, we add the effect of electron scattering on opacity (i.e., modified blackbody spectrum; *short-dashed line*). Radiation from the inner region is boosted toward higher energy. Finally, Comptonization is included in the computations (*solid line*). Comparing the solid and dot-dashed lines, the spectral hardening factor (the ratio of the color temperature to the effective temperature) at the innermost region is about 3.4. [See the electronic edition of the Journal for a color version of this figure.]

super-Eddington accretion rate:  $L \sim 2.6L_{\text{Edd}}$  for the relativistic corrected spectrum, while  $L \sim 5.1L_{\text{Edd}}$  for the noncorrected spectrum.

Next, we add the effect of electron scattering on opacity (i.e., the modified blackbody spectrum; *short-dashed line*). Finally, Comptonization is included in the computations (*solid line*). Radiation from the inner region is boosted toward higher energy by a factor of  $\sim 3.4$  (the ratio of the color temperature to the effective temperature, called the “spectral hardening factor”; see, e.g., Shimura & Takahara 1995) in comparison with the dot-dashed line. This factor can be estimated if one compares the color temperature (*dot-long-dashed line*) and the effective temperature (*solid line*) in the bottom panel of Figure 5. With the effects of electron scattering (opacity and Comptonization), we get more gradual slopes in soft X-ray than in the original spectra (*dotted line and long-dashed line*). The effect of Comptonization is included in the slim disks for the first time here (see also Shimura & Manmoto 2003; Wang & Netzer 2003).

For the spectrum with all the effects ( $\dot{m} = 1000$  and  $\alpha = 0.1$ ), the contribution from each radial component is shown in Figure 8:  $r \geq 10^3$ ,  $r = 10^3$ – $100$ ,  $100$ – $10$ ,  $10$ – $5$ ,  $5$ – $3$ , and  $r \leq 3r_{\text{Sch}}$ , respectively (*thin solid lines*). For comparison, we also draw the spectra without the effects of electron scattering (but with the relativistic correction) by thin dot-dashed lines. The spectral hardening factor of each spectrum is 1.3, 1.7, 2.3, 2.9, 3.4, and 4.0 for each radial region, respectively. This means that the inner emission suffers more spectral shift by electron scattering.

Figure 9 shows the  $\alpha$  dependency of the emergent spectra with  $\alpha = 0.1$ ,  $0.01$ , and  $10^{-3}$ . The arrows indicate the change of spectra with increasing  $\alpha$ . The meanings of two kinds of lines (solid and dot-dashed) are the same as Figure 7. Without the effects of electron scattering, the spectra are

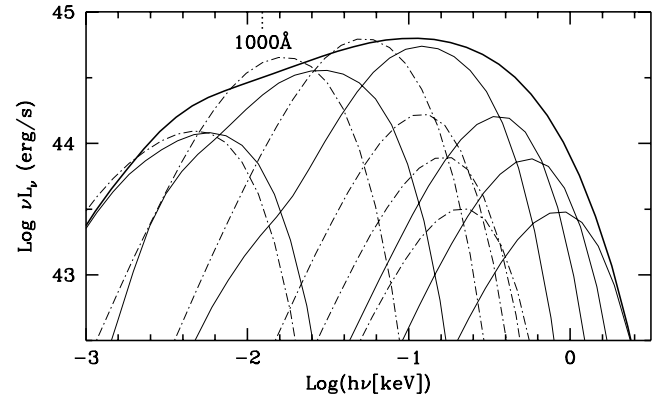


FIG. 8.—Contributions from different radii:  $r \geq 10^3$ ,  $r = 10^3$ – $100$ ,  $100$ – $10$ ,  $10$ – $5$ ,  $5$ – $3$ , and  $r \leq 3r_{\text{Sch}}$ , from left to right, for  $M_{\text{BH}} = 10^{6.5} M_{\odot}$ ,  $\dot{m} = 1000$ , and  $\alpha = 0.1$ . The thick solid line shows the spectrum from the entire radius with all the spectral effects the same as in Fig. 7, while six thin solid lines mean the spectra from the different radial regions above. For comparison, we also draw the spectra without the effects of electron scattering (but with the relativistic correction) by thin dot-dashed lines. The “spectral hardening factor” of each spectrum is 1.3, 1.7, 2.3, 2.9, 3.4, and 4.0 for each radial region, respectively. [See the electronic edition of the Journal for a color version of this figure.]

almost identical. Spectral boosting by electron scattering is quite  $\alpha$  sensitive. Since  $\tau_{\text{es}}/\tau_{\text{abs}} \propto \alpha^{1/8}$ , an increase of  $\alpha$  results in an increase of the surface temperature  $T$  (eq. [16]), so we get more spectral boosting. Previous models with the effect of electron scattering in opacity (Szuszkiewicz et al. 1996; Wang et al. 1999) employ a low viscosity parameter  $\alpha = 0.001$ , in order to guarantee that the flow is effectively optically thick. Such a low  $\alpha$  means that the spectral distortion by electron scattering is very small (Fig. 9).

Figure 10 shows the emergent spectra with  $M_{\text{BH}} = 32 M_{\odot}$  and  $\alpha = 0.1$ . Meanings of the lines are the same as in Figure 7. Those spectra can correspond to those of some ULXs/microquasars. The spectral hardening factors are around 1.3, 1.9, and 6.5 for  $\dot{m} = 1$ , 10, and 1000, respectively. For  $\dot{m} = 100$ , it is quite difficult to measure it, since the spectrum is highly distorted (see § 4.2 for the reason). The  $\dot{m}$  dependency presented here is qualitatively the same as the  $10^{6.5} M_{\odot}$  results. Some more details are shown in § 4.2. Because of the reduction of  $(\bar{\kappa}_{\text{abs},0}/\bar{\kappa}_{\text{ff},0})$  in the  $10^{1.5} M_{\odot}$  calculations (§ 2.1), the effects of electron scattering on spectral boosting are enhanced relative to  $10^{6.5} M_{\odot}$  results (Figs. 7 and 12). Shimura & Takahara (1995) derived the spectral hardening factors to be  $\sim 1.7$  for  $\dot{m} = 1$  and  $\sim 1.9$  for  $\dot{m} = 10$ , using the

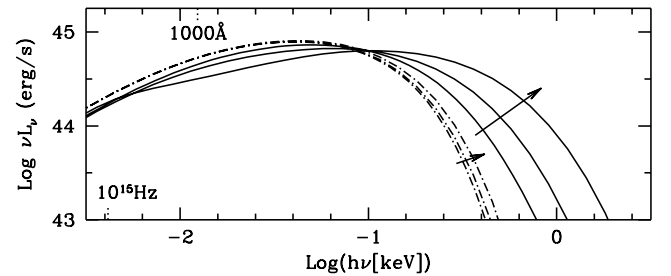


FIG. 9.—Spectra with three different values of  $\alpha$ : 0.1, 0.01, and  $10^{-3}$ . The arrows indicate the change of spectra with increasing  $\alpha$ . The meanings of two kinds of lines (solid and dot-dashed) are the same as in Fig. 7. Without the effects of electron scattering, the spectra are almost identical. Spectral boosting by electron scattering is quite  $\alpha$  sensitive. [See the electronic edition of the Journal for a color version of this figure.]



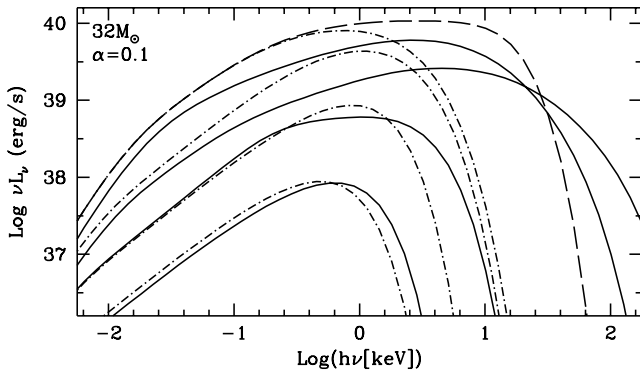


FIG. 10.—Emergent spectra from the face-on slim disks (solid lines) with  $M_{\text{BH}} = 32 M_{\odot}$  and  $\alpha = 0.1$ . Accretion rates  $\dot{m}$  used for the computations are 1, 10, 100, and 1000, from bottom to top. The meanings of lines are the same as in Fig. 7. Roughly, the spectral hardening factor is 1.3, 1.9, and 6.5 for  $\dot{m} = 1, 10$ , and 1000, respectively. Shimura & Takahara (1995) reported that the spectral hardening factor is  $\simeq 1.7$  for  $\dot{m} = 1$  and  $\simeq 1.9$  for  $\dot{m} = 10$  ( $M_{\text{BH}} = 1.3\text{--}10 M_{\odot}$ ), with a weak  $M_{\text{BH}}$  dependency ( $\sim M_{\text{BH}}^{0.1}$ ). [See the electronic edition of the *Journal* for a color version of this figure.]

radiative transfer computations including Comptonization. It is often assumed that the vertical distribution of the heating rate is proportional to the volume gas density (Ross, Fabian, & Mineshige 1992; Shimura & Takahara 1993, 1995). Our results are consistent with their values; thus, the method used here for spectral calculations seems to work quite well. Strong disk Comptonization, which is turned on at very high state in a couple of microquasars, is suggested by Kubota (2001) and Kubota, Makishima, & Ebisawa (2001a). We note that the inferred bolometric luminosity assuming the standard  $T_{\text{eff}}(r)$  profile (e.g., Mitsuda et al. 1984) will be underestimating the true disk luminosity (perhaps by a factor of 1.5–2), since super-Eddington accretion flows have flatter (in  $\nu L_{\nu}$  plot) spectra than the standard accretion disk (Fig. 10).

#### 4. OBSERVATIONAL TESTS OF THE MODEL

Here we will test the models with the data of AGNs, for which detailed data at both optical/UV and X-ray bands are available and some sorts of  $M_{\text{BH}}$  estimations have been developed.

##### 4.1. The Object Ideal for the Test

Objects ideal for the test should have the highest  $\dot{m}$ , since we expect the largest difference in spectral shape from the spectrum of the standard accretion disk. In addition, the high  $\dot{m}$  indicates a geometrically thick accretion flow (Fig. 5), and then the self-obscuration may happen (Fukue 2000). If we observe the innermost region of those highest  $\dot{m}$  objects (detections with soft X-ray will indicate it), it implies that we are looking at the flow almost face-on. Thus, we can neglect the longitudinal Doppler effect (Doppler boosting), which is an annoying effect in the model fitting. (We simply estimate the luminosity as  $4\pi d_L^2$  times flux, neglecting the inclination of the disk/flow. The inferred luminosity will overestimate the true luminosity somewhat in the case of a concave flow geometry due to the self-irradiation [Fukue 2000; Misra & Sriram 2003].) Another reason to favor a large  $\dot{m}$  is that the effective optical depth of the flow with  $\dot{m}$  of 100 can be smaller than 1, so the radiative cooling rate (eq. [6]) would not be accurate in that case. We should select

even higher  $\dot{m}$  objects. Another requirement for ideal test objects is that they should also harbor as small  $M_{\text{BH}}$  as possible. Small enough  $M_{\text{BH}}$  allows the accretion disk to become hot enough for the emission from the innermost part of the flow to be easily observable in the soft X-ray band.

In terms of the temporal analysis, low- $M_{\text{BH}}$  selection is also desirable in order to recognize the temporal behavior characteristic of the slim disk. The accretion timescale at  $r \lesssim 10 R_{\text{Sch}}$  and  $r \lesssim 30 R_{\text{Sch}}$  will have the order of a typical exposure time of X-ray satellite ( $\sim 10$  ks) for  $\dot{m} = 100$  and 1000, respectively (Fig. 4). Thus, the slim disk is expected to change its dynamics within one observation. To select the candidates for high- $\dot{m}$  and low- $M_{\text{BH}}$  objects, we plot  $B$ -band luminosity of each active nuclei  $\nu L_{\nu}(B)$  as a function of  $M_{\text{BH}}$  as follows.

There are several ways to estimate  $M_{\text{BH}}$  of AGNs: (1) The reverberation mapping technique provides physically meaningful  $M_{\text{BH}}$  estimation [ $M_{\text{BH}}(\text{rev})$ ; e.g., Kaspi et al. 2000], although the method is quite time consuming (an order of a year). Now,  $M_{\text{BH}}(\text{rev})$  estimations for AGNs whose  $\text{FWHM}(\text{H}\beta) < 2000 \text{ km s}^{-1}$  have been obtained for nine objects (Kaspi et al. 2000). (2) An easier way is the one assuming some photoionization models for  $\text{H}\beta$  lines [ $M_{\text{BH}}(\text{ph})$ ; Wandel, Peterson, & Malkan 1999]. The two estimations agree with each other quite well. The method utilizes the regression line between the size of broad-line regions  $R_{\text{BLR}}$  and  $\nu L_{\nu}(5100 \text{ \AA})$ , determined in the reverberation mapping (Kaspi et al. 2000):

$$R_{\text{BLR}} = 32.9 [\nu L_{\nu}(5100 \text{ \AA}) / (10^{44} \text{ ergs s}^{-1})]^{0.7} \text{ lt-days}.$$

(3) Nelson (2000) and Ferrarese et al. (2001) found that the  $[\text{O III}]$  line width or the stellar velocity dispersion,  $\sigma$ , is correlated with  $M_{\text{BH}}(\text{rev})$  in AGNs and that they overlap the bulge mass-to-BH mass correlation in nonactive galaxies (Gebhardt et al. 2000; Ferrarese & Merritt 2000). Thus, the  $[\text{O III}]$  width also provides an estimate of  $M_{\text{BH}}$ ,  $M_{\text{BH}}([\text{O III}])$ . We use the regression reported in equation (2) of Wang & Lu (2001), which was derived from  $M_{\text{BH}}(\text{rev})$  or  $M_{\text{BH}}(\text{ph})$  versus  $[\text{O III}]$  width of the narrow-line and broad-line AGNs:

$$M_{\text{BH}}([\text{O III}]) = 10^{7.78} [\text{FWHM}([\text{O III}]) / 2.35 / (200 \text{ km s}^{-1})]^{3.32} M_{\odot}.$$

We confirmed that an alternative regression (eq. [3]) in Wang & Lu (2001) does not change the result significantly.

There is some scatter around the regression lines, in both the  $R_{\text{BLR}}$  versus  $\nu L_{\nu}(5100 \text{ \AA})$  diagram and the  $M_{\text{BH}}$  versus  $[\text{O III}]$  width plot. To minimize uncertainty, we estimate  $M_{\text{BH}}$  from the geometric mean of the three estimations, namely, the square root of the product of  $M_{\text{BH}}(\text{rev})$  and  $M_{\text{BH}}([\text{O III}])$ , or that of  $M_{\text{BH}}(\text{ph})$  and  $M_{\text{BH}}([\text{O III}])$ . In general, those evaluations agree with each other quite well:  $\langle [\log_{10} M_{\text{BH}}(\text{rev or ph}) - \log_{10} M_{\text{BH}}([\text{O III}])]^2 \rangle = 0.54$ . The SDSS Early Data Release spectra also show a similar scatter:  $\sigma \simeq 0.67$  in  $\log_{10} M_{\text{BH}}(\text{ph})$  (Boroson 2003). In some objects without two available estimations, we use either of the three.<sup>2</sup>

<sup>2</sup> We use  $M_{\text{BH}}([\text{O III}])$  for IC 3599 and 2E 1346+2646 and  $M_{\text{BH}}(\text{rev})$  for PG 0052+251, PG 1226+023, PG 1426+015, PG 1617+175, and PG 1700+518.

For some NLS1s, the [O III] line can be deconvolved into two components (Véron-Cetty, Véron, & Gonçalves 2001 and references therein), namely, the broad, blueshifted one and the narrower one with the same redshift as other lines. The latter seems to arise from clouds showing normal galactic rotation. For  $M_{\text{BH}}([\text{O III}])$ , the latter [O III] width is used as Wang & Lu (2001) did, if the [O III] line is deconvolved into the two components. However, for I Zw 1, it is known that neither of the two components appears at the galaxy redshift (Phillips 1976; Véron-Cetty et al. 2001): both components seem to show outflows. Therefore, this object is omitted in our plot.

In general, NLS1s have a narrower [O III] line width ( $\lesssim 300 \text{ km s}^{-1}$ ) than BLS1s. To take account of a possible overestimation of the [O III] width due to the moderate spectral resolution ( $\sim 200 \text{ km s}^{-1}$ ), Wang & Lu (2001) divide the [O III] width listed in Véron-Cetty et al. (2001) by a factor of 1.3. We follow the same procedure. Spectroscopic observations with higher spectral resolution and, as for I Zw 1, a careful analysis of the two [O III] components will be required in the future to obtain a regression with smaller scatter.

In addition to the objects and data in Wang & Lu (2001), Nelson (2000), and Kaspi et al. (2000), the following well-known NLS1s that are not tabulated in the literature are added, namely, several NLS1s with the *ASCA* observations (see Leighly 1999b). Some NLS1s show giant amplitude (a factor of  $\sim 10$ –100) X-ray variability. We also add such objects to our sample (see § 6.1 for more details). Table 1 lists the added objects: eight objects from Leighly (1999b) and four from Grupe, Thomas, & Beuermann (2001). In total, we have 100 objects: 74 narrow and 26 broad objects. We note that the current sample is far from a complete sample by any means.

The Galactic extinction is corrected using a standard extinction curve (Savage & Mathis 1979). For all the conversion between optical bands and for the *K*-correction, it is assumed that  $f_\nu \propto \nu^{-0.5}$  (e.g., Kaspi et al. 2000). Accuracy of the optical photometric data must be considered carefully: e.g., the nuclear fraction of the measured luminosity is 0.64–0.97 for  $\nu L_\nu(B) \geq 10^{44.2} \text{ ergs s}^{-1}$  sources (Surace, Sanders, & Evans 2001). Less luminous sources would contain less nuclear fraction. The optical variability is of smaller amplitude than X-ray variability.

Figure 11 exhibits the  $M_{\text{BH}}$  versus  $\nu L_\nu(B\text{-band})$  plot. This plot will be useful to estimate the order of  $\dot{m}$  [roughly  $\propto L_\nu(B)/M_{\text{BH}}$ ] in a sample of objects. The closer to the line of  $L_{\text{Edd}}$  (dashed line), the higher  $\dot{m}$  such objects will have. NLS1s/narrow-line QSOs seem to have higher  $\dot{m}$  than BLS1s/QSOs. If we do not apply the [O III] width correction by a factor of 1/1.3 for the Wang & Lu (2001) sample, most NLS1s (54 out of 74) shift to the right (larger  $M_{\text{BH}}$ ) by 0.2 dex. Still there is the systematic difference of  $\dot{m}$  between NLS1s/narrow-line QSOs and BLS1s/QSOs. The objects' names are indicated for several outliers. PG 1700 and PG 1704 are also pointed out as the highest  $\dot{m}$  objects by Collin et al. (2002), who estimated  $\dot{m}$  of 34 AGNs from the optical luminosity and  $M_{\text{BH}}(\text{rev})$ .

The best high- $\dot{m}$ , low- $M_{\text{BH}}$  target is PG 1448+273 ( $z = 0.065$ ). The inferred BH masses are  $M_{\text{BH}}(\text{ph}) = 8.4 \times 10^6 M_\odot$  and  $M_{\text{BH}}([\text{O III}]) = 6.3 \times 10^5 M_\odot$ . We thus estimate  $M_{\text{BH}}$  as  $10^{6.4} M_\odot$ . It has  $\nu L_\nu(B) = 10^{44.4} \text{ ergs s}^{-1}$ . The FWHM widths of H $\beta$  and [O III] are 820 and 155  $\text{km s}^{-1}$ , respectively (Stirpe 1990; Véron-Cetty et al. 2001). The optical spectrum shows no evidence for contamination from the host galaxy into the optical luminosity, and it is not expected in *B* band (Stirpe 1990). These widths are still narrower than typical NLS1s, indicating that this object will

TABLE 1  
ADDITIONAL NLS1s AND A BLS1

| Objects Name                | $z$   | H $\beta^a$<br>FWHM<br>( $\text{km s}^{-1}$ ) | $m_V$ | References | $A_V^b$ | [O III] <sup>a</sup><br>FWHM<br>( $\text{km s}^{-1}$ ) | $L_B^c$<br>( $\text{ergs s}^{-1}$ ) | $R_{\text{BLR}}$<br>(lt-days) | $M_{\text{BH}}(\text{ph})^d$ | $M_{\text{BH}}([\text{O III}])^d$ |
|-----------------------------|-------|---|-------|------------|---------|--|-------------------------------------|-------------------------------|------------------------------|-----------------------------------|
| PHL 1092.....               | 0.396 | 1790  | 17.0  | 1          | 0.13    | ...  | 45.0                                | 168.2                         | 7.90                         | ...                               |
| RX J0439.7–4540.....        | 0.224 | 1010  | 16.6  | 2          | 0.03    | 1020   | 44.7                                | 92.2                          | 7.14                         | 8.90                              |
| NAB 0205+024 (Mrk 586)..... | 0.155 | 1050  | 15.4  | 3          | 0.10    | ...  | 44.9                                | 125.0                         | 7.30                         | ...                               |
| PKS 0558–504.....           | 0.137 | 1250  | 15.0  | 4          | 0.15    | ...  | 44.9                                | 140.6                         | 7.51                         | ...                               |
| 1H 0707–495.....            | 0.041 | 1050  | 15.7  | 4          | 0.32    | 1516 <sup>e</sup>                                      | 43.7                                | 18.5                          | 6.47                         | ...                               |
| IRAS 13224–3809.....        | 0.067 | 650 <sup>f</sup>                              | 15.2  | 5          | 0.23    | 810  | 44.3                                | 47.8                          | 6.47                         | 8.56                              |
| IRAS 13349+2438.....        | 0.108 | 2200  | 14.3  | 6          | 0.04    | ...  | 45.0                                | 147.4                         | 8.02                         | ...                               |
| IRAS 20181–2244.....        | 0.185 | 370   | 16.8  | 7          | 0.24    | 537  | 44.5                                | 71.0                          | 6.15                         | 7.97                              |
| RX J0134.2–4258.....        | 0.238 | 900   | 16.0  | 2          | 0.06    | 670  | 45.0                                | 150.6                         | 7.25                         | 8.29                              |
| WPVS 007.....               | 0.029 | 1620  | 14.8  | 2          | 0.04    | 320  | 43.6                                | 17.0                          | 6.81                         | 7.23                              |
| RX J2217.9–5941.....        | 0.160 | 1850  | 16.2  | 2          | 0.08    | 1075   | 44.6                                | 77.0                          | 7.59                         | 8.97                              |
| RX J2349.3–3125.....        | 0.135 | 5210  | 16.6  | 2          | 0.05    | 475  | 44.2                                | 46.0                          | 8.26                         | 7.80                              |

<sup>a</sup> Line widths of H $\beta$  and [O III] are taken from Leighly 1999b for the upper eight objects and from Grupe et al. 1999, with  $\sim 5 \text{ \AA} \sim 300 \text{ km s}^{-1}$  resolution, for the lower four objects.

<sup>b</sup> Galactic extinction  $A_V$  is derived from NED.

<sup>c</sup>  $\log_{10}[\nu L_\nu(B)]$ .

<sup>d</sup>  $\log_{10}(M_{\text{BH}}/M_\odot)$ .

<sup>e</sup> This [O III] width is uncertain as a result of low [O III] flux and contamination from Fe II blends (K. M. Leighly 2001, private communication). Then, we estimate  $M_{\text{BH}}$  from  $M_{\text{BH}}(\text{ph})$  alone.

<sup>f</sup> This H $\beta$  width may be underestimated, since there seems to be some contamination of the narrow H $\beta$  line arising from starbursts of the host galaxy (K. M. Leighly 2001, private communication).

REFERENCES.—(1) Véron-Cetty & Véron 2001. (2) Grupe et al. 1999. (3) Korista 1991. (4) Remillard et al. 1986. (5) Young et al. 1999. (6) Mason et al. 1995. (7) Elizalde & Steiner 1994.

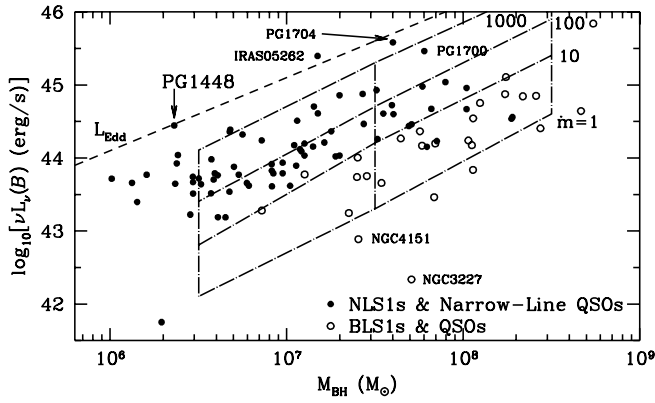


FIG. 11.— $B$ -band luminosity of active nuclei as a function of  $M_{\text{BH}}$ . Data are derived from Wang & Lu (2001), Nelson (2000), and Kaspi et al. (2000). NLS1s and narrow-line QSOs are denoted by filled circles, while BLS1s and QSOs are plotted by open circles. Narrow-line objects show higher  $\dot{m}$  than broad-line objects on average. Among the low- $M_{\text{BH}}$ , higher  $\dot{m}$  NLS1s, PG 1448+273 is the candidate with highest  $\dot{m}$ . Then, this object can be desirable to test the overall slim disk model. Dashed lines are loci computed by the model for different  $\dot{m}$  with  $\alpha = 0.1$ . Optical flux has a very weak  $\alpha$  dependency (Fig. 9). Absolute  $B$ -band magnitude  $M_B$  of  $-23$  corresponds to  $\nu L_\nu(B)$  of  $10^{44.8}$  ergs  $\text{s}^{-1}$ . [See the electronic edition of the *Journal* for a color version of this figure.]

be one of the extreme NLS1s. We expect that the object will show the hottest accretion disk among the sample, which will enable us to investigate the nature of accretion flow unprecedentedly well with soft X-ray observations (*XMM-Newton*). No X-ray observations have been performed for this object except for *ROSAT* All-Sky Survey (RASS); the 0.1–2 keV photon index  $\Gamma$  is  $3.2 \pm 0.3$  ( $1\sigma$ ), and  $\nu F_\nu(2 \text{ keV})$  is  $(1.4 \pm 0.5) \times 10^{-12}$  ergs  $\text{s}^{-1} \text{cm}^{-2}$  (Walter & Fink 1993). There are no special remarks on this object in Grupe et al. (2001) where some objects showing strange variability during RASS observations are reported.

#### 4.2. Comparison of the Models with the Available Data

Now we compare our model spectra (§ 3.2) with the currently available, observed data of PG 1448+273 at optical–soft X-ray bands (Fig. 12). The standard disk model ( $\dot{m} \lesssim 10$ ) does not fit the broadband spectrum of PG 1448+273 (dot and a bow tie error); thus, a slim disk model is required. The soft X-ray photon index of PG 1448+273 ( $\Gamma \sim 3.2$ ) is larger than normal BLS1s (see, e.g., Boller et al. 1996) but is not the largest one among the NLS1s ( $\Gamma \sim 2.5$ –4.5).

Figure 12 exhibits a comparison of spectra between the optical ( $B$ -band) to soft X-ray (by RASS) observations and the models. Here  $M_{\text{BH}}$  is taken to be  $10^{6.5} M_\odot$  and  $\alpha = 0.1$  (top panel) or 0.01 (bottom panel). The corresponding  $\dot{m}$ -value for each line is shown in the figure. The spectral hardening factors for  $\alpha = 0.1$  cases are  $\sim 1.2$ , 1.3, and 3.4 for  $\dot{m} = 1$ , 10, and 1000, respectively, while  $\alpha = 0.01$  results indicate the factor to be  $\sim 2.8$  and 2.3 for  $\dot{m} = 100$  and 1000, respectively. The  $\dot{m} = 1000$  and  $\alpha = 0.1$  model with all the effects (solid line) has a problem: the soft X-ray spectrum is too boosted toward higher energy to explain the observed value. We found that the PG 1448+273 data are well fitted by a model with an extremely large accretion rate:  $\dot{m} = 1000$  and  $\alpha = 0.01$ . As far as the soft X-ray spectrum is concerned, both of the  $\dot{m} = 100$  and 1000 models with  $\alpha = 0.01$  can fit the data. Thus, it is very important to look at both optical/UV and soft X-ray bands. We note that most of the

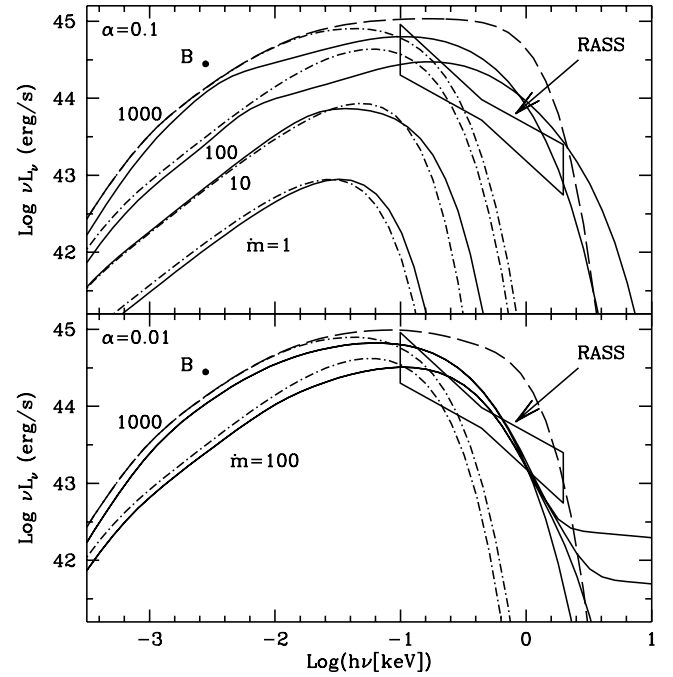


FIG. 12.—Spectral models of the face-on slim disk (solid lines), with  $M_{\text{BH}} = 10^{6.5} M_\odot$ , for the observed data of PG 1448+273 (dot and a bow tie; errors indicate  $1\sigma$  of  $\Gamma$  and flux). Accretion rates used for the computations are labeled. Bolometric luminosities  $L$  are 0.021, 0.21, 1.2, and 2.6 of  $L_{\text{Edd}}$  for  $\dot{m} = 1$ , 10, 100, and 1000, respectively. The meanings of lines are the same as in Fig. 7. The dot-dashed and long-dashed lines are computed without the effects of electron scattering: the relativistic correction is taken into account in the former, but not in the latter. *Top*: Cases with  $\alpha = 0.1$ . Roughly, the spectral hardening factor is 1.2, 1.3, and 3.4 for  $\dot{m} = 1$ , 10, and 1000, respectively. (For  $\dot{m} = 100$  it is difficult to measure it, since the spectrum is highly distorted. See the text for that reason.) To reproduce the optical flux,  $\dot{m} \geq 1000$  is required. The  $\dot{m} = 1000$  model with all the effects (solid line) has a problem: the soft X-ray spectrum is too boosted toward higher energy to explain the observed value. *Bottom*: Same as the top panel, except for  $\alpha = 0.01$  here. Models for  $\dot{m} = 100$  and 1000 are shown, with the resultant spectral hardening factors of  $\sim 2.8$  and 2.3, respectively. For presentation purposes, we add a hard X-ray power law with a photon index of 2.15 for each spectrum, with the 3000 Å–2 keV spectral index of 1.6. It is found that the  $\dot{m} = 1000$  case reproduces the observed broadband spectrum quite well. [See the electronic edition of the *Journal* for a color version of this figure.]

dissipated energy is advected and swallowed into the BH as trapped photons. This is the first example where optical–soft X-ray spectral distributions of NLS1s are explained by models. The dashed lines are the curves based on the previous computation of the slim disk (Minoshige et al. 2000) with  $\dot{m} = 1000$ , which turned out to have difficulty in explaining the soft X-ray luminosity/spectral slope. In the bottom panel, spectra with an additional hard X-ray power law are also shown, for presentation purposes. The photon index of 2.15 (Brandt, Mathur, & Elvis 1997; Leighly 1999b), with the 3000 Å–2 keV spectral index of 1.6 (Brandt, Laor, & Willis 2000), is used.

Figure 12 also exhibits the  $\dot{M}$  dependence of the model spectra with a fixed  $M_{\text{BH}}$ . We recall that  $\tau_{\text{eff}} \leq 1$  at the inner region, with  $\dot{m} = 100$  and  $\alpha = 0.1$ . Because of the exponential term in equation (16) (the effect of the finite  $\tau_{\text{eff}}$ ), the surface temperature  $T$  drastically increases with the parameter set. The spectral hardening factor, the degree of spectral boosting relative to the model without electron scattering, is indeed enhanced and becomes more strongly radius dependent (see § 3.4 of Shimura & Takahara 1995 for  $r$  dependency



of the factor in sub-Eddington AGN disks) in the  $\dot{m} = 100$  case than the  $\dot{m} = 1000$  result. Up to  $\dot{m} \leq 10$ , the peak frequency of the disk emission ( $T_{\text{in}}$ ) varies with  $\dot{M}$  in a similar fashion to that of the standard accretion disk:  $T_{\text{in}} \propto M_{\text{BH}}^{-1/2} \dot{M}^{1/4} \propto M_{\text{BH}}^{-1/4} \dot{m}^{1/4}$ . Above that accretion rate, there is a jump in  $T_{\text{in}}$ , as a result of the  $\dot{m}$ -sensitive spectral boosting via electron scattering. Such a jump does not happen without electron scattering effects (*dot-dashed lines*).

With  $\dot{m} \geq 100$ ,  $T_{\text{in}}$  saturates, as found in previous works (Wang et al. 1999; Watarai et al. 2000; Mineshige et al. 2000).

As shown above, we have established that the slim disk model is promising for PG 1448+273 for *B*-band and RASS data ( $\dot{m} = 1000$  producing  $2.6L_{\text{Edd}}$ ). This is the first success in reproducing optical-soft X-ray emission simultaneously. To verify and constrain our model further, we need a much higher signal-to-noise ratio and a broader bandpass obtainable with *XMM-Newton*. We will show the detailed comparison between the model and the data, which will be obtained by our approved observation (PI: T. Kawaguchi), in a future paper. In addition, whether we are able to fit the spectra at different flux states with the same  $M_{\text{BH}}$  provides a strong constraint on the accretion models.

#### 4.3. Predicted X-Ray Features

Below we state several features predicted by the model. These properties will be judged by future observations.

*Is the spectrum distorted as a result of electron scattering?*—The most distinguishable feature of the slim disk is the soft X-ray spectrum (soft excess or soft X-ray hump) from the innermost region of the disk. The soft excess may not be fitted well by the so-called multicolor disk spectra, since the slim disk model predicts that the soft X-ray emission is significantly distorted as a result of the strong radius-dependent, spectral hardening factor at a certain range of  $\dot{m}$  ( $\dot{m} = 100$  with  $\alpha = 0.1$ ; Fig. 12, *top panel*). Such a power-law-like soft excess was recently reported in a couple of NLS1s, Ton S180 (Vaughan et al. 2002) and Mrk 478 (Marshall et al. 2003) with  $\Gamma \sim 3$  and  $\sim 1.5$  for soft and hard X-ray, respectively.

*Intrinsic spectral features.*—The temperature of the innermost region of NLS1s with  $\dot{m} \gtrsim 1000$  seems to be around  $10^6$  K. Those objects tend to have weaker coronae than coronae of low- $\dot{m}$  objects. Then, it can be possible to observe the intrinsic spectral features (bound-free and bound-bound) of the accretion flow in the soft X-ray band. Such features have commonly been attributed to “warm absorbers.” However, the strong Comptonization (Fig. 2) may smear those features (see Shimura 2000). Some discussions on possible disk emission features in *XMM* data have appeared recently (Branduardi-Raymont et al. 2001; Mason et al. 2003).

*Does the color temperature change with flux?*—The color temperature of the radiation from the innermost disk ( $T_{\text{in}}$ ) may vary with flux significantly (Fig. 12). Such a behavior of the slim disk (significant change of  $T_{\text{in}}$  associated with less change in  $L$ ) is expected to occur at  $\dot{m} = 10$ – $100$ , as a result of the  $\dot{m}$ -sensitive electron scattering. If we detect the significant  $T_{\text{in}}$  change, distinct from the simplest (without the effects of electron scattering) standard disk model ( $T_{\text{in}} \propto L^{1/4}$ ), it is evidence for strong electron scattering and hence (see Fig. 2) is an indication of super-Eddington accretion in NLS1s.

It should be stressed that a similar  $T_{\text{in}}$  change has been observed in ULXs/microquasars (see Makishima et al. 2000): e.g., Mizuno, Kubota, & Makishima (2001) found that three ULXs exhibit  $T_{\text{in}} \propto L^{1/2}$ , which is different from the relation in the standard disk,  $T_{\text{in}} \propto L^{1/4}$ .

*Is photon trapping important, or does convection dominate?*—Another expectation from the slim disk model is that the soft excess might be reduced at higher  $\dot{m}$  as a result of advection (photon trapping). The accretion timescale will become shorter than the timescale of photon diffusion (Fig. 4). We may therefore expect less soft X-ray excess-to-optical flux ratio for extremely high  $\dot{m}$  than for a moderately large  $\dot{m}$  case. That could be verified from the combination of OM and EPIC observations, since optical/UV radiation suffers less from the photon trapping. Absence of this effect will mean that the convective energy transport in the disk is more efficient than the radiative one.

## 5. GROWTH TIMESCALE OF BLACK HOLES

The elapsed time since the gas fueling started will have the order of  $M_{\text{BH}}/\dot{M}$  ( $=0.5\dot{m}^{-1}$  Gyr) unless a sudden change of accretion rate occurs. Thus, NLS1s and narrow-line QSOs could be the key objects for figuring out what turned on the efficient gas accretion toward the central BHs. As described in the previous section, we found that some of them, including PG 1448+273, have an extremely high accretion rate:  $\dot{m} \approx 1000$ . This implies that the object is really young: its age inferred from  $M_{\text{BH}}/\dot{M}$  is about  $10^6$  yr. As a result of the rapid growth of  $M_{\text{BH}}$ , such a high- $\dot{m}$  stage will be a quite short phase.

It may be important to note that some ULXs exhibit extended optical nebulae (Pakull & Mirioni 2002). Assuming that a nebula is a remnant of a supernova-like event, they estimate the age of one ULX as  $\sim 1$  Myr based on the size of the nebula ( $\sim 400$  pc in diameter), expansion velocity, and  $H\beta$  luminosity.

## 6. DISCUSSION

### 6.1. Highly Variable AGNs

Some NLS1s show giant amplitude (a factor of  $\sim 10$ – $100$ ) X-ray variability; short-term ( $\lesssim 1$  day) variabilities in IRAS 13224–3809 (Boller et al. 1997; see also Otani et al. 1996), PHL 1092 (Forster & Halpern 1996; Brandt et al. 1999), RX J2217.9–5941 (Grupe et al. 2001), and Mrk 766 (Leighly et al. 1996; Grupe et al. 2001); and long-term (approximately years) variabilities in NGC 4051 (Guainazzi et al. 1998; Uttley et al. 1999), RE J1237+264 (=IC 3599; Brandt, Pounds, & Fink 1995; Grupe et al. 1995a; Komossa & Bade 1999), 1H 0707–495 (Leighly et al. 2002), and WPVS 007 (Grupe et al. 1995b), etc. To investigate the physics and nature behind these phenomena, we have added such objects into Figure 11: three NLS1s, WPVS 007 (=1RXS J003915.6–511701; Grupe et al. 1995b), RX J0134.2–4258 (Grupe et al. 2000), and RX J2217.9–5941, and one BLS1, RX J2349.3–3125 (Grupe et al. 2001). RX J1304.2+0205 and HS 1702+32 (Grupe et al. 2001) are not included since there are no optical data available.

When  $\dot{m}$  goes up, a shorter accretion timescale is associated with a higher radial velocity (Figs. 3 and 4). This suggests that such specific NLS1s (and one BLS1) might have the highest  $\dot{m}$  among all NLS1s. Some of the highly variable

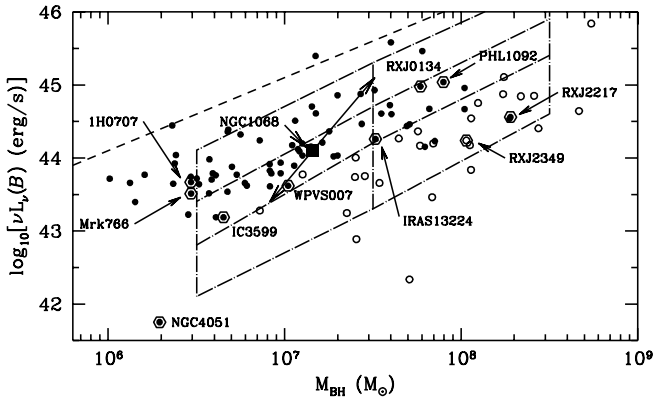


FIG. 13.—Resultant distribution of highly variable/transient AGNs (hexagons). They do not belong to the highest  $\dot{m}$  group. Instead, it seems that such objects are located at the intermediate region where the two classes merge. A large filled square denotes NGC 1068 (§ 6.3). [See the electronic edition of the *Journal* for a color version of this figure.]

and transient AGNs (e.g., NGC 4051) may be relevant to obscuration (e.g., Brandt & Gallagher 2000)

The resultant distributions of those AGNs are shown in Figure 13 together with other objects. It turns out that they do not belong to the highest  $\dot{m}$  group. This is true even if we use one specific  $M_{\text{BH}}$  estimation among the three, rather than the geometric mean. Instead, it seems that such highly variable objects are located at the intermediate region where the two classes merge ( $3 \lesssim \dot{m} \lesssim 300$ ). If this is true, the distribution may indicate that such high-amplitude variability is linked with a transience between a standard disk and a slim disk as a result of the thermal instability (Honma et al. 1991a, 1991b; Leighly et al. 2002). Further studies with a sample including more transient NLS1s are required to examine this hypothesis.

Janiuk, Czerny, & Siemiginowska (2002) discuss the thermal instability in terms of transitions of microquasars. Transitions seen in some ULXs (Kubota et al. 2001b) can also be relevant to the instability.

### 6.2. Photon Trapping

As shown in Figure 4, the diffusion timescale of photons becomes longer than the accretion timescale (photon trapping). We expect that the diffusion approximation (eq. [6]) should provide a reasonable estimation for the cooling rate, although Ohsuga et al. (2002) argue that it might not always be true for super-Eddington accretion rates. A similar trapping phenomenon can be seen for the neutrino trapping in a newly born neutron star (proto-neutron star) associated with a Type II (core-collapse) supernova. The diffusion timescale of neutrinos from the dense core (seconds) is longer than the dynamical timescale of collapse or bounce shock around the neutrino sphere (1–10 ms; see Burrows 1990 for a review). Numerous studies (e.g., Janka & Hillebrandt 1989; Mezzacappa et al. 1998), adopting the (flux-limited) diffusion approximation and Monte Carlo simulations to treat the neutrino leakage, have been made for calculating the inner structure and light curve of the neutrino flux from a (convective) proto-neutron star. The long history of this field would help to consider the cooling rate in super-Eddington accretion flows.

The inner structure of a magnetized accretion flow will be highly inhomogeneous (e.g., Machida, Hayashi, &

Matsumoto 2000; Kawaguchi et al. 2000). Photons inside the flow tend to escape by passing through a low-density region (see Begelman 2001). Therefore, the degree of photon trapping, and thus that of advection, might be reduced when we take this into account. However, the photon diffusion timescale (Fig. 4, *dotted lines*) is much longer than the dynamical timescale ( $\Omega_K^{-1}$ ; *dot-dashed line*). Since the inner inhomogeneity will change within the timescale of  $\Omega_K^{-1}$ , photons will still have difficulty in escaping from the flow. A lower  $\alpha$  enhances the deviation of the two timescales.

### 6.3. NGC 1068: A Type 2 NLS1?

Here we briefly discuss the accretion rate of a well-known Seyfert 2 galaxy, NGC 1068. The relatively narrow H $\beta$  line and significant Fe II multiplets in the polarized emission from NGC 1068 (Miller, Goodrich, Mathews 1991) lead people to suspect it as a type 2 counterpart of NLS1s.

For NGC 1068, the mean [O III] width ( $\sim 1150 \text{ km s}^{-1}$ ) cannot be used for  $M_{\text{BH}}$  determination, since NLR clouds seem to suffer from the interaction with the jet (Dietrich & Wagner 1998). The lowest FWHM ( $\sim 200 \text{ km s}^{-1}$ ) [O III] clouds seem to be consistent with rotation around the nucleus, and the FWHM width of the line complex from those clouds is about  $210 \text{ km s}^{-1}$  (Dietrich & Wagner 1998). Consequently, the implied  $M_{\text{BH}}([\text{O III}])$  is  $4.2 \times 10^6 M_\odot$ . In addition, its polarized H $\beta$  line width is  $\sim 3000 \text{ km s}^{-1}$  (Miller et al. 1991), and its intrinsic optical luminosity  $[\nu L_\nu(B)]$  was estimated as  $\sim 10^{44.1} (f_{\text{refl}}/0.01)^{-1} \text{ ergs s}^{-1}$ , assuming the fraction of nuclear flux reflected into our line of sight  $f_{\text{refl}}$  to be 0.01 (Pier et al. 1994). Therefore,  $M_{\text{BH}}(\text{ph}) = 5.1 \times 10^7 (f_{\text{refl}}/0.01)^{-0.7} M_\odot$ . The geometric mean is  $10^{7.2} (f_{\text{refl}}/0.01)^{-0.35} M_\odot$ . We note that  $f_{\text{refl}}$  is thought to be between 0.05 (Bland-Hawthorn, Sokolowski, & Cecil 1991) and 0.001 (Bland-Hawthorn & Voit 1993). The inferred  $M_{\text{BH}}$  is consistent with the  $M_{\text{BH}}$  estimated from water masers in the central parsec,  $(1\text{--}2) \times 10^7 M_\odot$  (Greenhill & Gwinn 1997).

The filled square in Figure 13 indicates the location of NGC 1068, showing that it indeed has a high  $\dot{m}$  as NLS1s. The error bar shown here arises from the uncertainty of  $f_{\text{refl}}$  alone.

### 6.4. Comparison with the QSO Composite Spectrum

NLS1s are the dominant source of diffuse EUV photons in the local universe (Edelson et al. 1999). To examine the contribution of NLS1s in the distant, young universe, we need to understand the shape of the EUV spectrum as functions of  $M_{\text{BH}}$  and  $\dot{M}$ .

In order to recognize the difference in spectral energy distributions between NLS1s and QSOs, we plot the QSO composite spectrum by dotted lines (Zheng et al. 1997; Laor et al. 1997; Telfer et al. 2002) on our model spectra ( $M_{\text{BH}} = 10^{6.5} M_\odot$ ,  $\dot{m} = 100$  and 1000 with  $\alpha = 0.01$ ) in Figure 14. Following Laor et al. (1997), the vertical normalization of the composite spectrum is chosen to match with a representative NIR luminosity of nearby PG quasars, but readopting a Hubble constant of  $75 \text{ km s}^{-1} \text{ Mpc}^{-1}$  (namely, we divide by 2.25 from the spectrum in Fig. 6 of Laor et al. 1997). Although the  $\dot{m} \sim 1000$  period will be a quite short phase and thus rare, the phase with  $\dot{m} \sim 100$  will be common in NLS1s and narrow-line QSOs (Fig. 11). As shown in Figure 14, the two types of objects (NLS1s and QSOs) show quite different distributions. The ratio of the EUV

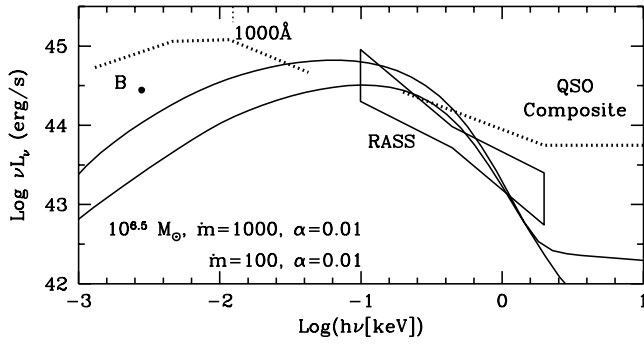


FIG. 14.—Comparison between the spectral models for NLS1s (solid lines;  $\dot{m} = 100$  [lower] and  $1000$  [upper] with  $M_{\text{BH}} = 10^{6.5} M_{\odot}$  and  $\alpha = 0.01$ ) and the QSO composite spectrum (dotted lines; Zheng et al. 1997; Laor et al. 1997; Telfer et al. 2002). Observational data for PG 1448+273 are also shown for presentation purposes. The two types of objects show quite different distributions. EUV luminosity is comparable in the NLS1 case ( $\dot{m} = 1000$ ) and the QSO spectrum, while optical and X-ray ones are very different. [See the electronic edition of the Journal for a color version of this figure.]

luminosity to optical ones and the EUV-to-X-ray ratio are really different in the high- $\dot{m}$  systems and QSOs. The EUV luminosity is comparable in the  $\dot{m} = 1000$  case and the QSO spectrum, while the EUV spectral slopes are not similar. The slope in EUV band plays an important role in indicating to what extent EUV photons penetrate into primordial gas clouds against self-shielding (e.g., Tajiri & Umemura 1998). Similar comparison can be seen when one plots the QSO composite spectrum onto the broadband spectrum of another NLS1, Mrk 478, in Marshall et al. (1996).

### 6.5. Other Perspectives

As prescribed in § 5, NLS1s can be in the younger phase of central BH formation/evolution. Mathur (2000) discusses the scenario in the context of gas content and metal richness of some NLS1s. If the “young AGN” hypothesis is valid, NLS1s provide us a good sample for studying the evolution and formation of massive BHs residing in the center of galaxies. Krongold, Dultzin-Hacyan, & Marziani (2001) compared the environments of NLS1s with those of BLS1s based on the Digitized Sky Survey, finding no statistical difference between the two. We will need much better spatial resolution to observe disturbances on host galaxies that may feed BHs and ignite AGN activity, such as a ripple structure, tidal tail, nucleus bar, and so on. Our forthcoming observation of nearby NLS1s with the University of Hawaii 2.2 m telescope (PI: K. Aoki) will assess the validity of this idea.

With recent intensive studies, it has been established that mass of the galactic spheroid component (galactic bulge or elliptical galaxy itself) is strongly correlated with  $M_{\text{BH}}$  in in-active galaxies and AGNs (Gebhardt et al. 2000; Ferrarese & Merritt 2000; Nelson 2000). The tight correlation indicates that the growth of spheroid mass (in other words, formation of spheroids) and growth of  $M_{\text{BH}}$  (formation of BHs) are triggered by the same origin, or it implies that either controls the other growth/formation. The origin of the link is still unclear. Two opposite extremal ideas can be that (1) jet/outflow due to gas accretion onto the central BH may govern the formation of spheroid (Silk & Rees 1998), i.e., BHs are made before the bulge growth; and (2)

radiation drag by massive stars during the bulge formation can fuel the gas toward the central BH (Umemura 2001), resulting in bulges formed prior to BH growth. Deep, optical/NIR, off-nuclear spectroscopic observations of spheroids (bulges) associated with the youngest AGNs will reveal the origin of the close correlation. The time lag between the epochs of the bulge and BH growth could be recognized, depending on the spectral features of the bulges we shall obtain. It will promote insights into why the two massive (but with enormously different physical sizes) systems coevolve.

## 7. SUMMARY

We have examined the effects of electron scattering (opacity and Comptonization) and the relativistic correction (gravitational redshift and transverse Doppler effect) on the emergent spectra from super-Eddington accretion flows (the so-called slim disks) onto nonrotating BHs for  $M_{\text{BH}} = 10^{1.5}$  and  $10^{6.5} M_{\odot}$ .

The effective optical depth of the flow can be less than unity for  $\dot{m} \equiv \dot{M}/(L_{\text{Edd}}/c^2) = 100\text{--}1000$  with  $10^{1.5} M_{\odot}$  and for  $\dot{m} = 100$  with  $10^{6.5} M_{\odot}$ , if  $\alpha \geq 0.1$ . An improvement in the knowledge of the cooling rate will be required in those parameter sets. Although  $\dot{m}$  dependency and the radial profile of each physical quantity in the super-Eddington flow are different from the standard disk, the  $M_{\text{BH}}$  dependencies of the two accretion modes are almost identical. The  $\alpha$  dependency is also similar, except for the innermost region ( $r \lesssim 10r_{\text{Sch}}$ ). Narrow-line QSOs will be desirable laboratories for studying the self-gravity of the flow via optical/NIR observations.

With  $\dot{m} \geq 100$ , the spectral hardening factor via electron scattering is  $\sim 2.3\text{--}6.5$ . The color temperature of the innermost radiation ( $T_{\text{in}}$ ) is not proportional to  $L^{0.25}$ , as would be expected from the simplest standard accretion disk, as a result of the  $\dot{m}$ -sensitive spectral hardening factor. In the face-on view, there is no jump of  $T_{\text{in}}$  if we do not take the  $\dot{m}$ -sensitive electron scattering into account.

The improved spectral model has been applied to the optical-soft X-ray emission from NLS1s, for which  $M_{\text{BH}}$  are now estimated by a couple of ways, to evaluate their accretion rates  $\dot{m}$ . We have picked up one NLS1, PG 1448+273 with an inferred  $M_{\text{BH}}$  of  $10^{6.4} M_{\odot}$ , among the highest  $\dot{m}$  candidates. The broadband spectral distribution was successfully reproduced for the first time by the model with  $\dot{m} = 1000$  and  $\alpha = 0.01$ .

This extremely high  $\dot{m}$  implies that this object, as well as some other highest  $\dot{m}$  systems, is really young: its inferred age ( $M_{\text{BH}}/\dot{M}$ ) is less than  $10^6$  yr.

We have also briefly discussed the accretion rate  $\dot{m}$  of transient and highly variable NLS1s, finding that those are located at  $3 \lesssim \dot{m} \lesssim 300$ . Such a moderately high accretion rate can indicate that this variability is relevant to the thermal instability. A possible type 2 counterpart of NLS1s, NGC 1068, seems to have  $\dot{m}$  similar to NLS1s.

A more accurate estimate for absorption opacity, for which we assume 30 times free-free opacity in this study for simplicity, is required for better spectral calculations. It is because the absorption opacity determines the location of the last thermalization surface and hence the amount of redistributed photons by Comptonization. Moreover, viewing angle-dependent spectral models are needed.



This paper could never have been produced in this way without the use of the numerical code for solving the radial structure of super- and sub-Eddington accretion flows/disks that has been constructed and developed by Ryoji Matsumoto, Fumio Honma, and Mitsuru Takeuchi. The author wishes to thank Karen Leighly, Chiho Matsumoto, Ken-ya Watarai, Kentaro Aoki, Toshiya Shimura, Agata Róžańska, Jerzy Madej, Bożena Czerny, Ed Baron, Jean-Marc Huré, Suzy Collin, Chris Done, and Omer Blaes for helpful discussions. He also thanks Brandon Carter for patient and careful reading of the draft, Shin Mineshige for continuous encouragement, and an anonymous referee for careful reading and helpful comments. The main computations were performed at the Department of Physics and

Astronomy of the University of Oklahoma, when the author was there as a visiting graduate student. He appreciates all the members of the Department, especially C. Matsumoto and K. Leighly, for their hospitality. This research has made use of the NASA/IPAC Extragalactic Database (NED), which is operated by the Jet Propulsion Laboratory, California Institute of Technology, under contract with the National Aeronautics and Space Administration. This work was supported in part by the Research Fellowship of the Japan Society for the Promotion of Science (JSPS) for Young Scientists (4616) and by the JSPS Postdoctoral Fellowships for Research Abroad (464).

## REFERENCES

- Abramowicz, M. A., Czerny, B., Lasota, J. P., & Szuszkiewicz, E. 1988, *ApJ*, 332, 646  
 Begelman, M. C. 2001, *ApJ*, 551, 897  
 Begelman, M. C., & Meier, D. L. 1982, *ApJ*, 253, 873  
 Beloborodov, A. M. 1998, *MNRAS*, 297, 739  
 Beloborodov, A. M., Abramowicz, M. A., & Novikov, I. D. 1997, *ApJ*, 491, 267  
 Bland-Hawthorn, J., Sokolowski, J., & Cecil, G. 1991, *ApJ*, 375, 78  
 Bland-Hawthorn, J., & Voit, G. M. 1993, *Rev. Mexicana Astron. Astrofis.*, 27, 73  
 Boller, Th., Brandt, W. N., Fabian, A. C., & Fink, H. H. 1997, *MNRAS*, 289, 393  
 Boller, Th., Brandt, W. N., & Fink, H. H. 1996, *A&A*, 305, 53  
 Boroson, T. A. 2003, *ApJ*, 585, 647  
 Brandt, W. N., Boller, Th., Fabian, A. C., & Ruszkowski, M. 1999, *MNRAS*, 303, L53  
 Brandt, W. N., & Gallagher, S. C. 2000, *NewA Rev.*, 44, 461  
 Brandt, W. N., Laor, A., & Wills, B. J. 2000, *ApJ*, 528, 637  
 Brandt, W. N., Mathur, S., & Elvis, M. 1997, *MNRAS*, 285, L25  
 Brandt, W. N., Pounds, K. A., & Fink, H. 1995, *MNRAS*, 273, L47  
 Branduardi-Raymont, G., et al. 2001, *A&A*, 365, L140  
 Burrows, A. S. 1990, in *Supernovae*, ed. A. G. Petschek (Berlin: Springer), 143  
 Cheng, L., Wei, J., & Zhao, Y. 2002, *Chinese J. Astron. Astrophys.*, 2, 207  
 Colbert, E., & Ptak, A. 2002, *ApJS*, 143, 25  
 Collin, S., et al. 2002, *A&A*, 388, 771  
 Czerny, B., & Elvis, M. 1987, *ApJ*, 321, 305  
 Dietrich, M., & Wagner, S. J. 1998, *A&A*, 338, 405  
 Edelson, R., et al. 1999, *MNRAS*, 307, 91  
 Elizalde, F., & Steiner, J. E. 1994, *MNRAS*, 268, L47  
 Ferrarese, L., & Merritt, D. 2000, *ApJ*, 539, L9  
 Ferrarese, L., et al. 2001, *ApJ*, 555, L79  
 Forster, K., & Halpern, J. P. 1996, *ApJ*, 468, 565  
 Fukue, J. 2000, *PASJ*, 52, 829  
 Gebhardt, K., et al. 2000, *ApJ*, 539, L13  
 Goldreich, P., & Lynden-Bell, D. 1965, *MNRAS*, 130, 97  
 Greenhill, L. J., & Gwinn, C. R. 1997, *Ap&SS*, 248, 261  
 Grupe, D., Beuermann, K., Mannheim, K., Bade, N., Thomas, H.-C., de Martino, D., & Schwope, A. 1995a, *A&A*, 299, L5  
 Grupe, D., Beuermann, K., Mannheim, K., & Thomas, H.-C. 1999, *A&A*, 350, 805  
 Grupe, D., Beuermann, K., Mannheim, K., Thomas, H.-C., Fink, H. H., & de Martino, D. 1995b, *A&A*, 300, L21  
 Grupe, D., Beuermann, K., Thomas, H.-C., Mannheim, K., & Fink, H. H. 1998, *A&A*, 330, 25  
 Grupe, D., Leighly, K. M., Thomas, H.-C., & Laurent-Muehleisen, S. A. 2000, *A&A*, 356, 11  
 Grupe, D., Thomas, H.-C., & Beuermann, K. 2001, *A&A*, 367, 470  
 Guainazzi, M., et al. 1998, *MNRAS*, 301, L1  
 Halpern, J. P., & Oke, J. B. 1987, *ApJ*, 312, 91  
 Hayashida, K. 2000, *NewA Rev.*, 44, 419  
 Honma, F., Matsumoto, R., & Kato, S. 1991a, *PASJ*, 43, 147  
 Honma, F., Matsumoto, R., Kato, S., & Abramowicz, M. A. 1991b, *PASJ*, 43, 261  
 Hōshi, R. 1977, *Prog. Theor. Phys.*, 58, 1191  
 Huré, J.-M. 1998, *A&A*, 337, 625  
 Janiak, A., Czerny, B., & Siemiginowska, A. 2002, *ApJ*, 576, 908  
 Janka, H.-T., & Hillebrandt, W. 1989, *A&AS*, 78, 375  
 Kaspi, S., Smith, P. S., Netzer, H., Maoz, D., Jannuzi, B. T., & Givon, U. 2000, *ApJ*, 533, 631  
 Kato, S., Fukue, J., & Mineshige, S. 1998, *Black Hole Accretion Disks* (Kyoto: Kyoto Univ. Press)  
 Kawaguchi, T., Mineshige, S., Machida, M., Matsumoto, R., & Shibata, K. 2000, *PASJ*, 52, L1  
 Kawaguchi, T., Pierens, A., & Huré, J. M. 2003, *A&A*, submitted  
 Komossa, S., & Bade, N. 1999, *A&A*, 343, 775  
 Korista, K. T. 1991, *AJ*, 102, 41  
 Krongold, Y., Dultzin-Hacyan, D., & Marziani, P. 2001, *AJ*, 121, 702  
 Kubota, A. 2001, Ph.D. thesis, Univ. Tokyo  
 Kubota, A., Makishima, K., & Ebisawa, K. 2001a, *ApJ*, 560, L147  
 Kubota, A., et al. 2001b, *ApJ*, 547, L119  
 Laor, A., Fiore, F., Elvis, M., Wikes, B. J., & McDowell, J. C. 1997, *ApJ*, 477, 93  
 Laor, A., & Netzer, H. 1989, *MNRAS*, 238, 897  
 Leighly, K. M. 1999a, *ApJS*, 125, 297  
 ———. 1999b, *ApJS*, 125, 317  
 Leighly, K. M., Zdziarski, A. A., Kawaguchi, T., & Matsumoto, C. 2002, in *X-Ray Spectroscopy of AGN with Chandra and XMM-Newton*, ed. Th. Boller, S. Komossa, S. Kahn, & H. Kunieda (MPE Rep. 279; Garching: MPE), 259–262  
 Leighly, K. M., et al. 1996, *ApJ*, 469, 147  
 Liu, B. F., Mineshige, S., Meyer, F., Meyer-Hofmeister, E., & Kawaguchi, T. 2002, *ApJ*, 575, 117  
 Machida, M., Hayashi, M. R., & Matsumoto, R. 2000, *ApJ*, 532, L67  
 Madej, J. 1974, *Acta Astron.*, 24, 327  
 Makishima, K., et al. 2000, *ApJ*, 535, 632  
 Marshall, H. L., et al. 1996, *ApJ*, 457, 169  
 ———. 2003, *AJ*, 125, 459  
 Mason, K. O., et al. 1995, *MNRAS*, 274, 1194  
 ———. 2003, *ApJ*, 582, 95  
 Mathur, S. 2000, *MNRAS*, 314, L17  
 Matsumoto, R., Kato, S., Fukue, J., & Okazaki, A. T. 1984, *PASJ*, 36, 71  
 Matsumoto, R., Kato, S., & Honma, F. 1989, in *Theory of Accretion Disks*, ed. F. Meyer, W. J. Duschl, J. Frank, & E. Meyer-Hofmeister (Dordrecht: Kluwer), 167  
 Meyer, F., & Meyer-Hofmeister, E. 1994, *A&A*, 288, 175  
 Mezzacappa, A., et al. 1998, *ApJ*, 493, 848  
 Miller, J. M., Fabbiano, G., Miller, M. C., & Fabian, A. C. 2003, *ApJ*, 585, L37  
 Miller, J. S., Goodrich, R. W., & Mathews, W. G. 1991, *ApJ*, 378, 47  
 Mineshige, S., Kawaguchi, T., Takeuchi, M., & Hayashida, K. 2000, *PASJ*, 52, 499  
 Misra, R., & Sriram, K. 2003, *ApJ*, 584, 981  
 Mitsuda, K., et al. 1984, *PASJ*, 36, 741  
 Mizuno, T., Kubota, A., & Makishima, K. 2001, *ApJ*, 554, 1282  
 Narayan, R. 1997, in *IAU Colloq. 163, Accretion Phenomena and Related Outflows*, ed. D. T. Wickramasinghe, G. V. Bicknell, & L. Ferrario (ASP Conf. Ser. 121; San Francisco: ASP), 75  
 Narayan, R., & Yi, I. 1995, *ApJ*, 444, 231  
 Nelson, C. H. 2000, *ApJ*, 544, L91  
 Ohsuga, K., Mineshige, S., Mori, M., & Umemura, M. 2002, *ApJ*, 574, 315  
 Osterbrock, D. E., & Pogge, R. W. 1985, *ApJ*, 297, 166  
 Otani, C., Kii, T., & Miya, K. 1996, in *Röntgenstrahlung from the Universe*, ed. H. U. Zimmermann, J. E. Trümper, & H. Yorke (MPE Rep. 263; Garching: MPE), 491  
 Paczyński, B., & Wiita, P. J. 1980, *A&A*, 88, 23  
 Pakull, M. W., & Mirioni, L. 2002, in *New Visions of the X-Ray Universe in the XMM-Newton and Chandra Era*, in press  
 Phillips, M. M. 1976, *ApJ*, 208, 37  
 Pier, E. A., et al. 1994, *ApJ*, 428, 124  
 Pogge, R. W. 2000, *NewA Rev.*, 44, 381  
 Pounds, K. A., Done, C., & Osborne, J. 1995, *MNRAS*, 277, L5  
 Remillard, R. A., et al. 1986, *ApJ*, 301, 742  
 Roberts, T. P., & Warwick, R. S. 2000, *MNRAS*, 315, 98  
 Ross, R. R., Fabian, A. C., & Mineshige, S. 1992, *MNRAS*, 258, 189  
 Rybicki, G. B., & Lightman, A. P. 1979, *Radiative Processes in Astrophysics* (New York: Wiley)  
 Savage, B. D., & Mathis, J. S. 1979, *ARA&A*, 17, 73  
 Shakura, N. I., & Sunyaev, R. A. 1973, *A&A*, 24, 337  
 Shimura, T. 2000, *MNRAS*, 315, 345

- Shimura, T., & Manmoto, T. 2003, MNRAS, 338, 1013  
 Shimura, T., & Takahara, F. 1993, ApJ, 419, 78  
 Shimura, T., & Takahara, F. 1995, ApJ, 445, 780  
 Silk, J., & Rees, M. 1998, A&A, 331, L1  
 Stirpe, G. M. 1990, A&AS, 85, 1049  
 Surace, J. A., Sanders, D. B., & Evans, A. S. 2001, AJ, 122, 2791  
 Svensson, R. 1984, MNRAS, 209, 175  
 Szuszkiewicz, E., Malkan, M. A., & Abramowicz, M. A. 1996, ApJ, 458, 474  
 Tajiri, Y., & Umemura, M. 1998, ApJ, 502, 59  
 Takeuchi, M. 2000, poster paper presented at the Joint MPE/AIP/ESO Workshop on Observational and Theoretical Progress in the Study of Narrow-Line Seyfert 1 Galaxies  
 Telfer, R. C., et al. 2002, ApJ, 565, 773  
 Umemura, M. 2001, ApJ, 560, L29  
 Uttley, P., McHardy, I. M., Papadakis, I. E., Guainazzi, M., & Fruscione, A. 1999, MNRAS, 307, L6  
 Vaughan, S., et al. 2002, MNRAS, 337, 247  
 Véron-Cetty, M. P., & Véron, P. 2001, A&A, 374, 92  
 Véron-Cetty, M. P., Véron, P., & Gonçalves, A. C. 2001, A&A, 372, 730  
 Walter, R., & Fink, H. H. 1993, A&A, 274, 105  
 Wandel, A., Peterson, B. M., & Malkan, M. A. 1999, ApJ, 526, 579  
 Wandel, A., & Petrosian, V. 1988, ApJ, 329, L11  
 Wang, J.-M., & Netzer, H. 2003, A&A, 398, 927  
 Wang, J.-M., Szuszkiewicz, E., Lu, F.-J., & Zhou, Y.-Y. 1999, ApJ, 522, 839  
 Wang, T., Brinkmann, W., & Bergeron, J. 1996, A&A, 309, 81  
 Wang, T., & Lu, Y. 2001, A&A, 377, 52  
 Watarai, K., Fukue, J., Takeuchi, M., & Mineshige, S. 2000, PASJ, 52, 133  
 Watarai, K., & Mineshige, S. 2001, PASJ, 53, 915  
 Watarai, K., Mizuno, T., & Mineshige, S. 2001, ApJ, 549, L77  
 Young, A. J., et al. 1999, MNRAS, 304, L46  
 Zheng, W., Kriss, G. A., Telfer, R. C., Grimes, J. P., & Davidsen, A. F. 1997, ApJ, 475, 469